Tornadogenesis and Early Tornado Evolution in the El Reno, Oklahoma, Supercell on 31 May 2013

HOWARD B. BLUESTEIN

School of Meteorology, University of Oklahoma, Norman, Oklahoma

KYLE J. THIEM

National Weather Service, Peachtree City, Georgia

JEFFREY C. SNYDER

NOAA/OAR/National Severe Storms Laboratory, Norman, Oklahoma

JANA B. HOUSER

Department of Geography, Ohio University, Athens, Ohio

(Manuscript received 18 September 2018, in final form 11 March 2019)

ABSTRACT

This study documents the formation and part of the early evolution of a large, violent tornado near El Reno, Oklahoma, based on data from a mobile, polarimetric, rapid scan, X-band, Doppler radar. The main circulation associated with the tornado formed near the ground initially, ~90 s prior to the development of the vertically coherent vortex, which built upward through a vertical column of at least 3.5 km in less than 20 s, the update time of the Doppler radar data. Strong but broad rotation from 500 m to 1.5 km AGL also preceded the formation of the tornado at the surface by several minutes. A precipitation-loaded downdraft was observed in the right-forward flank of the storm, which could have enhanced evaporative cooling and allowed for a faster rate of baroclinic generation of low-level horizontal vorticity, while descending reflectivity cores in the right-rear quadrant might have enhanced low-level convergence to the rear of or along the leading edge of the rear-flank gust front. The intensification of the tornado occurred in spurts, not steadily, perhaps owing to surges in momentum at the surface associated with the precipitation-laden downdrafts. The tornado was highly tilted even when it was intensifying, calling into question the importance of a vertical juxtaposition of the mesocyclone aloft and the tornado at the surface. In this case study, while the development of a weak-echo hole was evidence of rotation, the absence of one did not mean that there was not a strong vortex, owing to the lofting of debris.

1. Introduction

To understand why tornadoes form and how they are related to processes occurring in their parent convective storms, high-resolution, near-surface observations of tornadogenesis are needed. Although numerical simulations can be used to do controlled experiments with varying environmental conditions (e.g., different wind shear and thermodynamic or buoyancy profiles) to assess the impact of such changes on the ability of a storm to produce a tornado, the experiments tend to be highly idealized. Previous simulations have also been unable to reproduce *both* the tornado and the storm with fine enough spatial resolution (grid spacing ~10 m) to resolve the tornado and involve approximate, bulk representations of boundary layer and microphysical processes. While much has been learned about the sources of vorticity in tornadoes and the physical processes that can affect tornadogenesis or low-level mesocyclogenesis in supercells from simulations

Supplemental information related to this paper is available at the Journals Online website: https://doi.org/10.1175/MWR-D-18-0338.s1.

Corresponding author: Howard B. Bluestein, hblue@ou.edu

DOI: 10.1175/MWR-D-18-0338.1

(e.g., Rotunno and Klemp 1985; Wicker and Wilhelmson 1995; Markowski and Richardson 2014; Dahl et al. 2014; Dahl 2015), it is important to be able to see what actually happens in nature and confirm that the simulations are realistic. For example, some finescale simulations show "rivers of vorticity" that form in response to surges of outflow at the surface (Dahl et al. 2014). These "rivers" may have been detected in previous single-Doppler analyses. One possible observation of a potential "river" came from a supercell in northwestern Oklahoma on 23 May 2008, within which small-scale vortices were observed to be moving into the hook echo of the storm (Snyder et al. 2013, their Fig. 11); other examples may be available but are not widely recognized. However, these rivers are yet to be seen definitively in multiple-Doppler-radar analyses, to the best of the authors' knowledge, perhaps because they are too small scale to be detected (owing to the inherent smoothing during the analysis procedure) or because they occur only over a very shallow layer near the ground, where data collection can be difficult.

Observations are needed in order to determine if there are features or processes that cannot be reproduced by numerical simulations; observations can be used to identify and, hopefully, improve physical processes that models cannot currently accurately represent. Houser et al. (2016), for example, found a weak-echo reflectivity band in a tornadic supercell, which may not yet have been reproduced in a numerical simulation owing to an inadequate representation of boundary layer turbulence in the model parameterizations. Although ground-based mobile Doppler radars have been used for two decades to provide observations of the hydrometeor and Doppler-velocity fields in tornadic supercells [summarized in Bluestein (2019)], relatively few datasets have been collected that actually document tornadogenesis (with no preceding tornadogenesis) *throughout much of the depth of the parent storm with both high temporal and spatial resolution.* Some of the most comprehensive published cases to date are from 30 May 2000 (Spencer, South Dakota; Alexander and Wurman 2005); 4 May 2007 (Greensburg, Kansas; Tanamachi et al. 2012); 23 May 2008 (Ellis–Plainville, Kansas; French et al. 2013; 5 June 2009 (Goshen County, Wyoming; Markowski et al. 2012b; French et al. 2013); and 24 May 2011 (El Reno, Oklahoma; French et al. 2013; Houser et al. 2015). Aside from the case discussed herein, others available to our group, but not yet analyzed/published, include 29 May 2012 (Kingfisher, Oklahoma; RaXPol), 29 May 2013 (SW OK; RaXPol), 16 May 2015 (Elmer, Oklahoma; RaXPol and MWR-05XP), and 14 May 2018 (Geuda Springs, Kansas; RaXPol).

Furthermore, resolving the three-dimensional wind field in supercells during tornadogenesis is challenging[1] because more than one radar must be situated at the proper locations such that the between-beam angle lies within a favorable range during tornadogenesis and the distance is near enough to the radar that spatial resolution is sufficient to resolve the wind field associated with the evolution of the vortex or vortices that evolve into a tornado. Since spatial resolution is lost during the multiple-Doppler synthesis of the wind owing to interpolation of the Doppler-wind field, rapid scan Doppler radar data (e.g., Wurman and Randall 2001; Bluestein et al. 2010; Kurdzo et al. 2017) from one radar without any smoothing is sometimes adequate to test hypotheses or theories concerning elementary aspects of tornadogenesis such as: At what levels does rotation associated with the nascent tornado and the tornado [tornadic vortex signature (TVS; Brown et al. 1978)] begin? Does the tornado propagate vertically or is it advected upward, downward, or both, and why? Are there any evolving features in the parent storm such as descending reflectivity cores (DRCs; Rasmussen et al. 2006), possibly associated with local downdrafts and momentum surges (e.g., Marquis et al. 2008; Skinner et al. 2014), and driven by precipitation loading or downward-directed perturbation pressure gradient forces (Byko et al. 2009), which have been related to tornadogenesis, at least circumstantially, some of the time (Kennedy et al. 2007)?

Trapp and Davies-Jones (1997) suggested that the dynamic pipe effect (Smith and Leslie 1978) may cause a strong vortex produced aloft to propagate downward. Other studies have shown that strong upward motion in a one-celled tornado (Tanamachi et al. 2012; Bluestein 2013) can advect the vorticity associated with the tornado upward. Alexander and Wurman (2005) analyzed mobile Doppler radar data showing the vertical evolution of Doppler shear signatures on time scales of minutes; other datasets on these time scales have been collected with a rapid-scan radar, scanning six levels (Wurman and Randall 2001). For these datasets, it was found that the Doppler shear signature contracted "simultaneously" with height throughout the observed depth of the vortex. In an examination of three cases using rapid scan Doppler radar (the Ellis–Plainville tornado of 23 May 2008, the

[1] A promising single-Doppler retrieval (SDVR) technique has been used to estimate the three-dimensional wind field in tornadic supercells (Liou et al. 2018) and others are being developed (A. Shapiro, University of Oklahoma, 2018, personal communication).

Goshen County tornado of 5 June 2009, and the El Reno tornado of 24 May 2011) French et al. (2013) found no evidence that the formation of a tornadic vortex signature (TVS) began at midlevels and then propagated downward with time as in early studies (Brown et al. 1978). Instead, the TVS either began at low levels and then propagated upward or formed nearly simultaneously (i.e., within the duration of a volume scan) in a column.

The main purpose of this paper is to document the formation and evolution of a violent tornado in a supercell using data from a mobile, rapid scan, polarimetric Doppler radar (RaXPol), which began data collection at close range prior to tornadogenesis and continued through a portion of the multiple-vortex stage of the tornado's evolution (Bluestein et al. 2015, 2018). This tornado was produced by a supercell near El Reno, Oklahoma, during the late afternoon of 31 May 2013 and is significant owing to its severity, extremely large size, and the casualties that resulted from it (e.g., Wurman et al. 2014). This is one in a series of papers dealing with radar data collected by RaXPol of this major tornado. Snyder and Bluestein (2014) evaluated several of the complexities involved with relating radar measurements to the enhanced Fujita (EF) scale. The mesoscale and synoptic-scale environments, as well as a storm-scale analysis of the formation and evolution of the parent supercell, are described in more detail in Bluestein et al. (2015); it was shown that the supercell evolved from a band of convective storms near the intersection of a dryline and cold front. Bluestein et al. (2016) examined an anticyclonic tornado in the El Reno storm that was described in relation to other anticyclonic tornadoes, which tend to occur along the end of the rear-flank gust front opposite to that where there is a mesocyclone or a cyclonic tornado. Wakimoto et al. (2015) described the behavior of some of the polarimetric variables with respect to the visual appearance and kinematic structure of the tornado during the most intense phase (after the times examined herein). Wakimoto et al. (2016) correlated a detailed damage survey with the mobile radar data. Bluestein et al. (2018) analyzed the behavior of multiple vortices observed during a ~90-s period in this tornado, and Witt et al. (2018) studied how hail signatures in the El Reno storm relate to observed hail sizes and locations with respect to features in the storm. *In this paper, we focus on storm-scale and substorm-scale features observed during tornadogenesis (~2251–2304 UTC) and subsequent, early tornado evolution (~2304–2314 UTC).* We refer the reader to Fig. 8 in Bluestein et al. (2015) for details on the overall evolution of the tornado and its track.

A brief review of RaXPol's characteristics, the methods employed to analyze the data, and deployment locations with respect to the tornado are given in section 2. An analysis of the evolution of the main tornado in the context of the storm-scale features of its parent supercell is given in section 3, and an analysis of the development and evolution (overall intensification) in the vertical of the Doppler shear signatures associated with the main tornado is described in section 4. Discrete bursts in precipitation at low levels in the right-forward and rear flanks of the storm are documented and discussed in section 5 in relation to vortex intensification. A summary of our findings and conclusions is found in section 6.

2. Radar and data overview

a. Deployments and scanning strategies

Details of field operations on 31 May 2013 are given in Bluestein et al. (2015) and Bluestein et al. (2018), and technical details about RaXPol are given in Pazmany et al. (2013). This study concerns itself mainly with the stationary part of the second deployment of the day (D2; 2247–2317 UTC; LDT is 5 h earlier), when a large, violent tornado formed to the west of the radar. D2 is divided into two parts because the scanning strategy was adjusted midway through the deployment. The "early" part of D2, during tornadogenesis but prior to the formation of the main, violent tornado, is from 2247:29–2305:39 UTC; the "later" part of D2, when the main tornado is intensifying is from 2305:55–2314:00 UTC. Analyses of data from the third deployment, when many secondary vortices were tracked, are given in Bluestein et al. (2018). Some information relevant to the field operations and data (i.e., radar characteristics and scanning strategies) discussed in this study is shown in Table 1.

b. Radar characteristics

While the information herein is also found in Bluestein et al. (2018), it is partially summarized here (and in Table 1) to aid the reader. The antenna was rotated rapidly, which resulted in beam smearing of about 0.4°–0.5° (Doviak and Zrnić 1993; Pazmany et al. 2013). Since the rotation rate and pulse repetition frequency were so high, pairs of pulses were transmitted at different frequencies separated by a pulse bandwidth (at 9.73 GHz ± 20 MHz) so that enough quasi-independent samples were collected to obtain what are considered to be low-variance estimates (e.g., Doviak and Zrnić 1993; Bringi and Chandrasekar 2001). During the first part of D2, 11 frequencies were used in succession, whereas 5 frequencies were used during the

TABLE 1. Scanning strategies and other characteristics of data collection during D2.

Operating frequency	9.73 GHz ± 20 MHz	
Antenna gain	44.5 dB	
Half-power (3dB) beamwidth	1°	
Dwell time	1° (radial)$^{-1}$	
Maximum antenna rotation rate	180° s^{-1}	
Peak transmitter power	20 kW	
	Early D2	Late D2
Time periods	2247:29–2305:39 UTC	2305:55–2314:00 UTC
Elevation angle	0°–20°	0°–5°
Increments in elevation angle	2°	1°
Updates	28–29 s	15–16 s
Range resolution	75 m	30 m
Gate spacing	45 m	30 m
Range from tornado center	9–9.4 km	4.9–8.5 km
Top of domain	3.2–3.4 km AGL	300–750 m AGL

second part of D2 (owing to the increase in pulse bandwidth associated with the decrease in pulse length used during these times). However, in tornadic debris, returns from the horizontal and vertical channels are poorly correlated, so data having each polarization may be averaged to increase the number of samples used to compute some of the radar moments (e.g., Doppler velocity; Snyder and Bluestein 2014). At 5–7.5-km range, where most of the radar measurements were made during D2, the azimuthal resolution was approximately 125–200 m. During the first part of D2 (i.e., generally before and through tornadogenesis), when deeper volumes were being collected, range resolution (pulse length) was 75 m with range gates spacing of 45 m; during the second part of D2, range resolution was 30 m with range–gate spacing of 30 m.

Although the characteristics of the radar system were sufficient to detect precipitation and debris motion at the range of the radar from the tornado, some regions, especially in clear air, were noisy enough that data had to be discarded. Data were manually edited to remove ground clutter and obvious noise using the third version of SOLO (Oye et al. 1995).

Because the pulse repetition time was 0.25 ms, velocity aliasing occurred at ±31 m s^{-1}, which at times was merely ¼ of the actual Doppler velocity. The Doppler velocity data were unfolded using de-aliasing algorithms in regions where the Doppler velocity spatial gradients were relatively weak. In regions where there were strong velocity gradients, such as those near the tornado, data were manually de-aliased, which is common in these types of datasets.

c. *Synthesis of vertical cross sections*

Vertical cross sections normal to the radar beam through the center of circulation were synthesized so that the vertical structure of the tornado could be determined. To do so, it had to be assumed that the tornado was steady during the time interval of data collection for one volume, which was ~30 s during the early part of D2 and ~15 s during the later part of D2 (Table 1). Since tornado evolution occurs on the order of 1–10 s (Bluestein et al. 2010), it is expected that there are some unavoidable errors as a result of very rapid evolution. Data synthesis included the interpolation of raw data onto a 3D Cartesian grid using a two-pass Barnes's scheme (Barnes 1964; Majcen et al. 2008) in the Observation Processing and Wind Synthesis (OPAWS; https://code.google.com/archive/p/opaws/) software package. The objective analysis parameters (Table 2) responsible for grid spacing and smoothing were chosen to preserve the high spatial resolution of the raw data as much as possible, while

TABLE 2. Parameters used for interpolation to a 3D Cartesian grid using a two-pass Barnes's objective analysis scheme.

	Early D2	Late D2
Δh (grid spacing in horizontal)	25 m	25 m
Δv (grid spacing in vertical)	50 m	50 m
κ_h (smoothing parameter in the horizontal)	0.025	0.010
κ_v (smoothing parameter in the vertical)	0.050	0.010
Resolution in azimuth	80–200 m	80–200 m
Resolution in elevation	160–400 m	80–200 m
Resolution along each radial	75 m	30 m

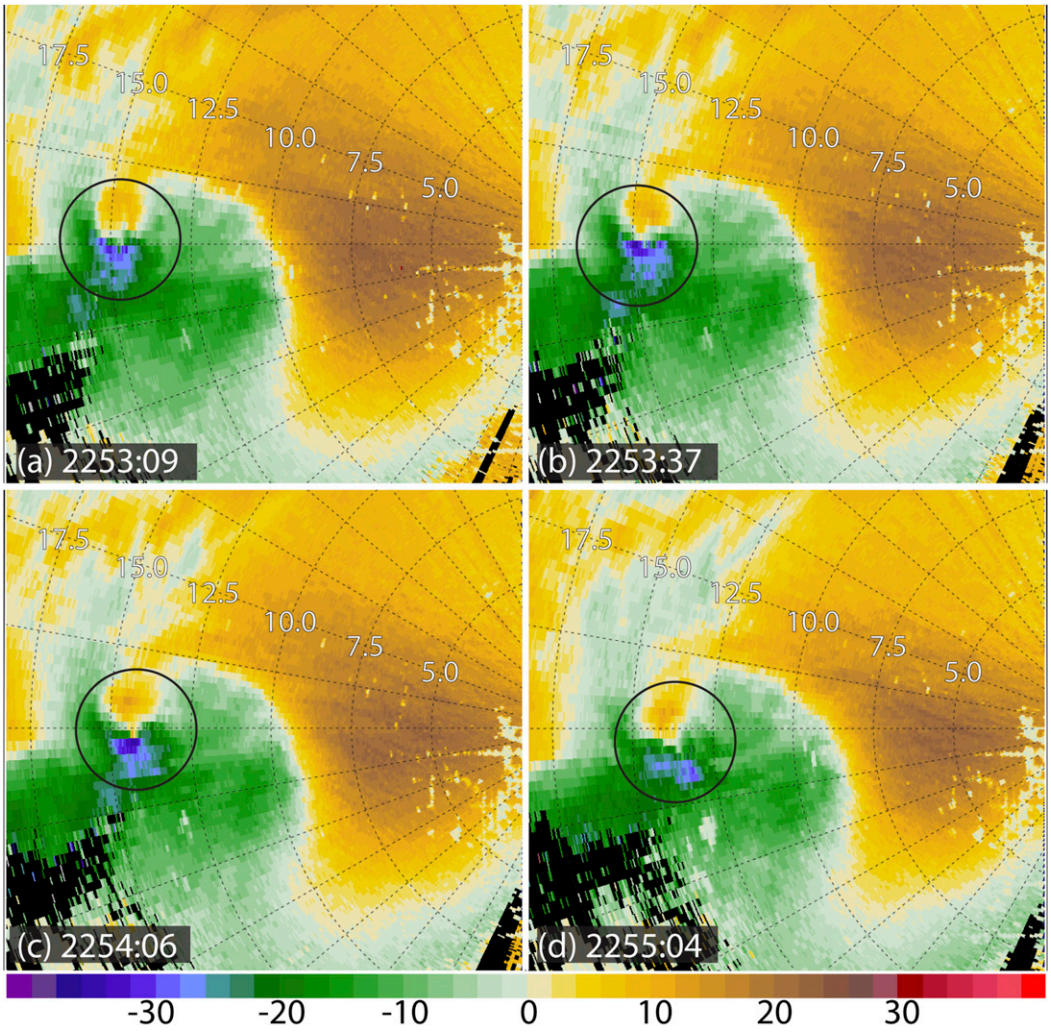

FIG. 1. Evolution of the vortex signature (circles) associated with the first, short-lived, tornado in the El Reno supercell: plan position indicators (PPIs) of RaXPol Doppler velocity ($m\,s^{-1}$) at 0° elevation angle at (a) 2253:09, (b) 2253:37, (c) 2254:06, and (d) 2255:04 UTC 31 May 2013. Range markers are shown every 2.5 km.

interpolating missing data or data that were removed because they were deemed too noisy or erroneous (Thiem 2016).

3. The evolution of the main tornado during D2

The focus in this section is the formation and evolution of the main, violent tornado during D2 and what transpired just prior to its formation. D2 began at 2247 UTC, when a mesocyclone in the southernmost cell of a broken line of storms was intensifying to the west of RaXPol (Bluestein et al. 2015). Approximately 8 min later (~2255 UTC), a weak (EF-0), short-lived (<1 min) tornado was reported ~16–17.6 km WSW of El Reno (*Storm Data*, NOAA), or about 14 km west of RaXPol (Fig. 1), near a cyclonic vortex signature that was most intense at the 0° elevation angle scans from ~2253:37–2254:06 UTC (Fig. 1); the vortex signature was weaker and broader both before and after these times.

The formation of the subsequent violent tornado and its evolution at 4° elevation (~500–600 m AGL) are depicted by radar reflectivity factor Z, Doppler velocity V, and copolar cross correlation coefficient ρ_{hv} at ~3–4 min intervals during D2, from 2300:00–2314:09 UTC in Fig. 2. Figure 2 also shows the track of the tornado (based on TVS locations) superimposed on the appearance of the radar reflectivity zoomed in on the tornado.

The main tornado was reported to have begun at 2303 UTC, though there were visual reports of the tornado 1 min earlier (Seimon et al. 2016) (Fig. 3) when the

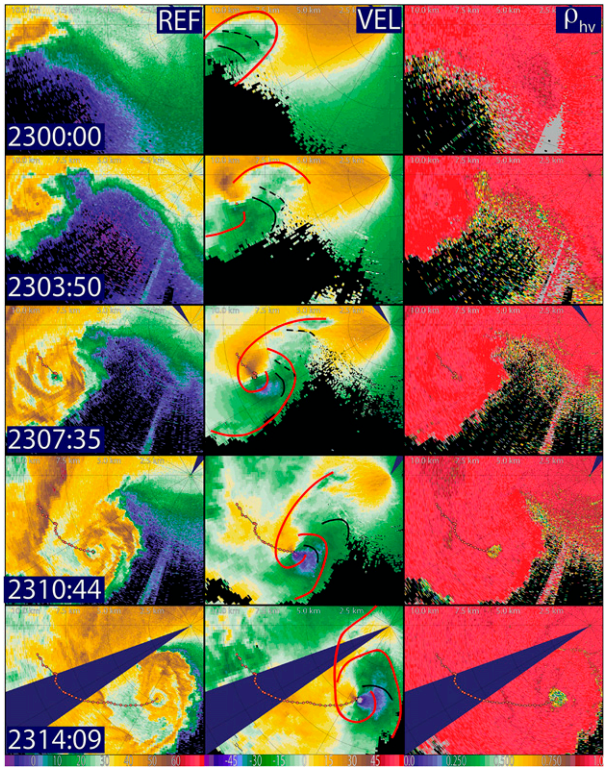

FIG. 2. Depiction of the formation and early evolution of the El Reno tornado during D2 as seen by RaXPol PPI sectors of (left) radar reflectivity (Z, in dBZ), (middle) dealiased Doppler velocity ($m\,s^{-1}$), and (right) copolar cross-correlation coefficient (ρ_{hv}) at 4° elevation angle, on 31 May 2013, at ~3.5-min increments (times shown at lower left in panels on leftmost column, in UTC). Range rings shown every 2.5 km. Red dots and connecting black line denote locations of tornado (i.e., the tornado track) based on the TVS location at 4° elevation angle. Curved, solid red lines mark the subjectively estimated locations of the forward flank gust front (FFGF) and the rear-flank gust front (RFGF), based on the Doppler velocity, ρ_{hv}, and spectrum width fields (not all shown). Solid black lines mark the subjectively estimated locations of secondary rear-flank gust fronts (SRFGFs), based on the Doppler velocity field; dashed black lines mark the locations of relatively weak SRFGFs.

FIG. 3. Video grab of the main tornado beginning at 2302:25 UTC, west of El Reno, Oklahoma. Photograph courtesy of H. Farrar.

shear resolved by the radar was weaker. The tornado tracked to the southeast initially but then slowed down and turned abruptly to the right (i.e., to the south) at ~2306 UTC. The tornado's track then turned gradually to the left, first to the southeast then to the east and east-northeast during the latter part of D2 (Fig. 2). A weak-echo hole (WEH) first appeared at 4° elevation angle ~3 min after the tornado first appeared as a vertically deep, continuous TVS (2307:35 UTC). The WEH is thought to represent the centrifuging radially outward of hydrometeors and debris (e.g., Dowell et al. 2005); the appearance of the WEH probably represents the intensification of the vortex. Alternatively, the WEH might be a manifestation of vertical motion within the tornado core (Tanamachi et al. 2012). Close to this time, a tornado debris signature (TDS) (e.g., Ryzhkov et al. 2005) first appeared (2310:44 UTC) as an approximately circular region of relatively low ρ_{hv}, which grew in size and built upward with time (not shown), as also noted by Houser et al. (2016) in another tornado (coincidentally also near El Reno, but on 24 May 2011).

Multiple surges in the rear-flank downdraft (RFD) region of the storm were also documented within this dataset [as evidenced by enhanced radial gradients of approaching V and locally enhanced lines of spectrum width associated with the enhanced radial gradients in V (not shown)], the most obvious of which are graphically represented in Fig. 2 by curved, solid black lines and weaker surges are indicated by a curved, dashed, black line, all located to the rear of the rear-flank gust front (RFGF). The changes in the direction of the track of the tornado occurred near the time when the scanning strategy was changed. These secondary rear-flank gust front (SRFGF) surges may have influenced the change of direction of the tornado track throughout D2 as the tornado first turned toward the south (~2307 UTC) and then gradually turned to its left (in a cyclonic path; ~2308–2314 UTC) as the surges transported high–momentum air initially to the southeast and then to the northeast. SRFGFs also appeared to also have affected the location of the RFGF relative to the tornado's location within the storm by pushing it out ahead of the tornado. By the end of D2, $V > 70\,m\,s^{-1}$ was measured within ~100 m of the surface (not shown), and EF3 damage was being produced (Bluestein et al. 2015; Wakimoto et al. 2015).

4. The vertical development of the TVS in the main tornado during D2

The period of the vertical development of the TVS/vortex signature during D2 is separated into two time

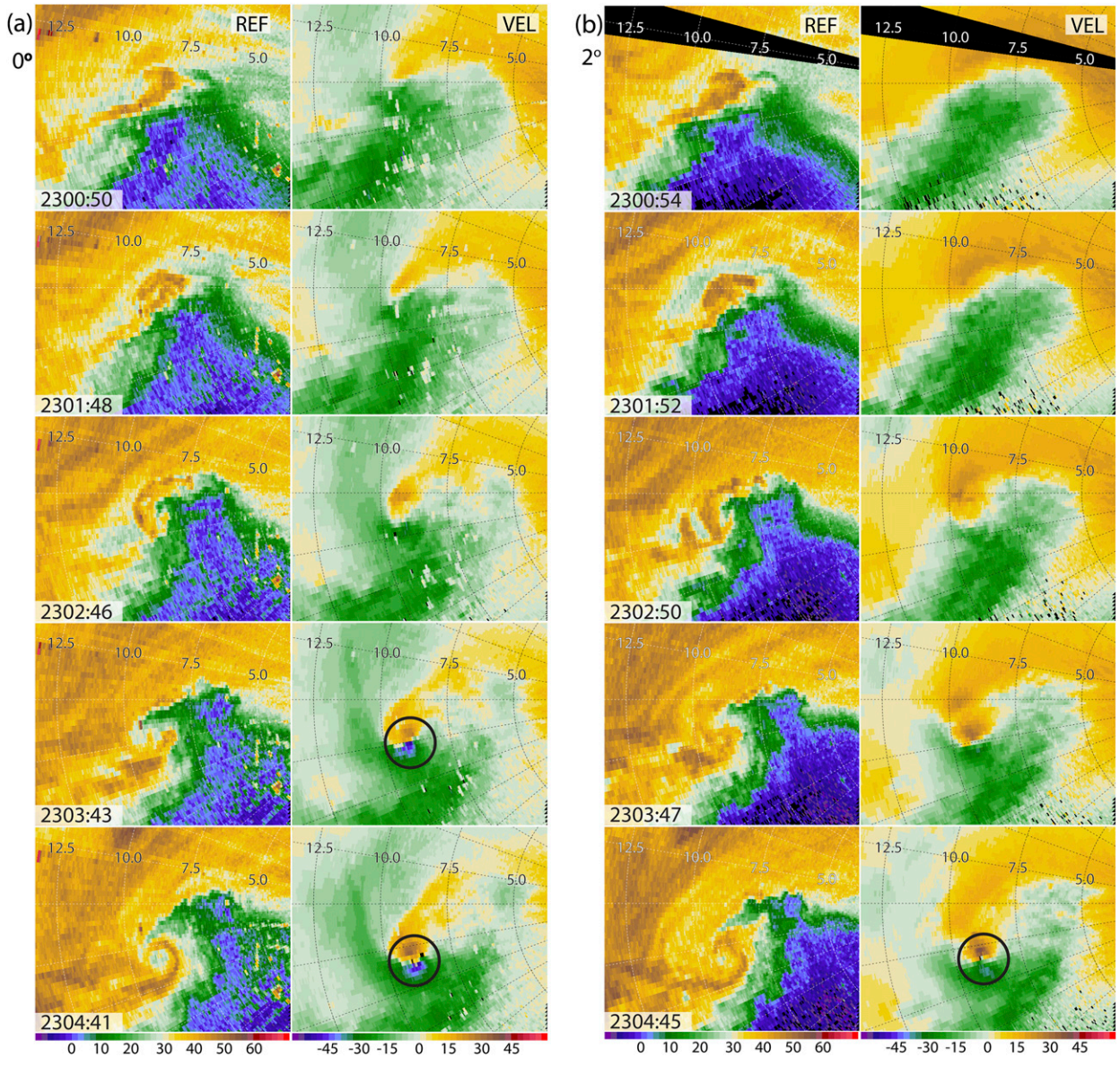

FIG. 4. The formation and early evolution of the El Reno tornado during D2 as depicted by radar reflectivity (dBZ) and dealiased Doppler velocity ($m\,s^{-1}$) from RaXPol at (a) 0° and (b) 2° elevation angle, shown every other volume scan (i.e., ~60 s, whereas volume update interval was ~30 s), at the times given in UTC on 31 May 2013. Range rings are indicated every 2.5 km. Well-defined shear couplets are enclosed by circles.

intervals, reflecting two distinctly different stages of the tornado (tornadogenesis and intensification/evolution) and the two different scanning strategies.

a. The early part of D2 (2247–2306 UTC): Tornadogenesis

The evolutions of the vortex shear signature (Brown et al. 1978) associated with the tornado at 0° and 2° elevation angles were different from each other (Fig. 4). At 2300:54 UTC at 2° elevation angle (~350 m AGL) there was just a broad mesocyclone shear signature (the difference in magnitude between the maximum receding and approaching velocities and/or the spacing between the maxima and minima were relatively small and large, respectively), which, by 2304:45 UTC, had developed into a tighter vortex signature (the difference in magnitude between the maximum receding and approaching velocities increased and the spacing between the maxima and minima were closer), having well defined, local maxima in approaching and receding Doppler velocity. This vortex signature was not near the location of the earlier vortex signature associated

with the first tornado (Fig. 1). At 0° elevation angle, however, a well-defined vortex signature (defined by nearby, distinct, relative maxima and minima in Doppler velocity) appeared earlier, at 2303:43 UTC. The intensity of the shear signature at the 0° elevation angle was also stronger than that at the 2° elevation angle.

The difference between the maximum outbound and inbound V ($\Delta V_{\max}$) of the vortex/circulation that evolved into the tornado can be combined with the distance between the maximum outbound and inbound Doppler velocities (a measure of the diameter of the core of the tornado;[D]) to calculate a proxy for the vertical vorticity in the tornado (e.g., Alexander and Wurman 2005; French et al. 2013; Houser et al. 2015). This methodology is not applicable when there are multiple vortices, but it is still valid for single-vortex tornadoes in which there is not solid-body rotation in between the center and the radius of maximum wind, as long as the azimuthal wind increases monotonically with distance from the center. Plots depicting $\Delta V_{\max}$ and D through the evolution of the tornado, in time and height, from the first detection of the vortex through the end of D2 are shown in Figs. 5–7. A $\Delta V_{\max}$ of at least 40 m s^{-1} has generally been used to mark the threshold for tornado intensity (e.g., Alexander and Wurman 2008), though for a radar or dataset having coarser spatial resolution (e.g., due to a broader beamwidth or greater distance between tornado and radar), the threshold may need to be lowered (e.g., French et al. 2013).

The vortex that developed into the main tornado was first detected near the ground (0° elevation angle) at 2300:21 UTC with a $\Delta V_{\max}$ of ~35 m s^{-1} (Figs. 4a, 5a). Around 2302 UTC, a ~2.5–3-km-wide vortex with $\Delta V_{\max}$ of ~60 m s^{-1} appeared aloft (i.e., in the layer from ~500 m to 1.75 km AGL). French et al. (2013) and Houser et al. (2015), in their analyses of rapid-scan data in other tornadoes, also noted a low-level mesocyclone found only between certain elevations prior to the development of the near-ground, tornado-strength vortex. The low-level (~500 m to 1.5 km AGL) mesocyclone had pseudovorticity

$$\zeta_{\text{pseudo}} = 2(\Delta V_{\max})/D \qquad (1)$$

(Figs. 5c, 7c)—a measure of the vertical vorticity of the tornado if it were axisymmetric—of ~0.05 s^{-1}, which remained approximately steady for a couple of minutes from ~2301:45–2303:30 UTC). As noted earlier, around ~2302:25 UTC, the tornado first appeared visually (Seimon et al. 2016) (Fig. 3). At this time, the only evidence of a TVS was found at 0° elevation angle (Figs. 4, 5a, 6). Above the surface, a relative minimum in

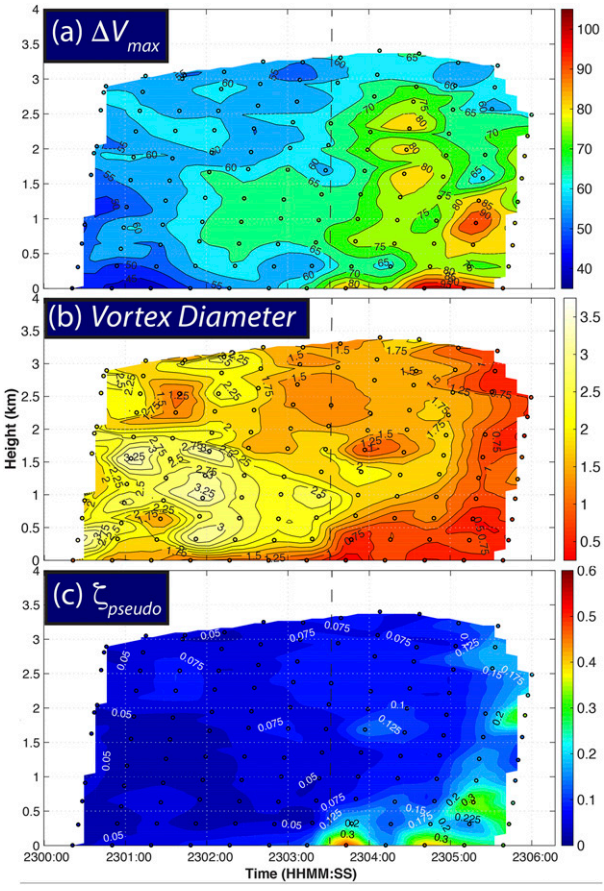

FIG. 5. The intensity of (a) the vortex shear signature ($\Delta V_{\max}$ in m s^{-1}) from RaXPol data, as a function of height ARL (above radar level, which is ~10 m AGL) (ordinate, in km) and time (abscissa, UTC) on 31 May 2013, well before and during tornadogenesis (vertical dashed line), during part of D2. The small circles denote the actual measurements, which were interpolated to a regular grid using cubic splines and displayed as a color-coded field. (b) The vortex diameter in km during and just before tornadogenesis, and (c) the pseudovorticity in s^{-1}. Range to the TVS was ~8–9 km.

$\Delta V_{\max}$ continued at ~250 m, in between the vortex near the ground and the low-level mesocyclone aloft. This vertical structure persisted for another minute. Around ~2303:30 UTC $\Delta V_{\max}$ suddenly increased both near the ground and in the 500-m–3-km layer (marked by a dashed line in Fig. 5). This time also coincided with a sudden decrease in vortex diameter from ~2.25 km to ~750 m just below 500 m AGL. At higher altitudes (e.g., above ~1.5 km AGL), D varied from ~1.5–2 km. Then, prior to 2305 UTC, $\Delta V_{\max}$ increased simultaneously near the ground and above 500 m, up to almost 3 km AGL. Following this increase, after 2305 UTC the vortex diameter decreased simultaneously up to the top of the domain (3 km AGL): Overall, D decreased

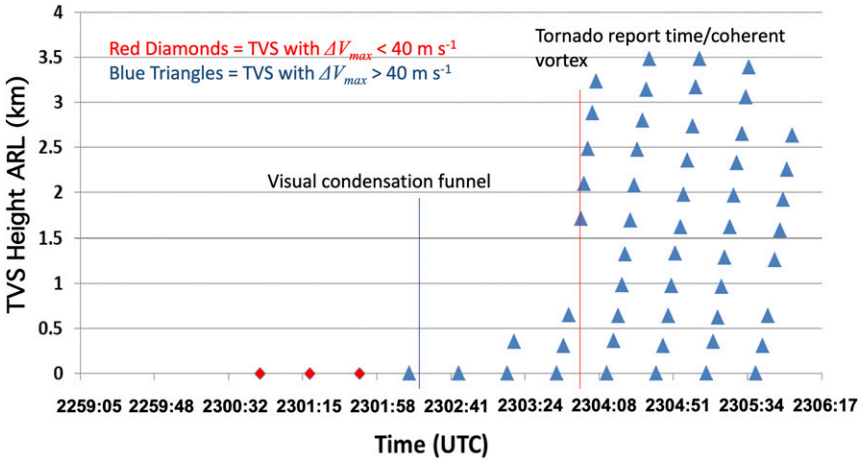

FIG. 6. Schematic of evolution of vortex signature and TVS evolution with respect to time and height. The red diamonds represent the pretornadic vortex signatures and the blue triangles represent the TVSs. Range to the TVS was ~8–9 km.

near the ground from ~2.25 km to 750 m (between ~2303:00 and 2304:30 UTC), while $\Delta V_{\max}$ increased from ~50 to ~100 m s^{-1}, and aloft to ~70–80 m s^{-1}, with one area > 90 m s^{-1} near 1 km AGL, separate from the near-ground maximum. The increases in ζ_{pseudo} seem to have come from both a contraction of the vortex diameter and an increase in Doppler velocity shear. While it appears in Fig. 5a that strengthening of the vortex signature occurred at 2° elevation first and then later at 0° elevation angle, it is emphasized that $\Delta V_{\max}$ is a measure of rotation, not the presence of a TVS; the shear is often relatively broad and does not meet the gate-to-gate shear requirements of a TVS. Figure 6 is shown specifically to depict the TVS evolution in height and time as distinct from the evolution of shear on any scale.

In summary, the development of the tornado occurred near the ground, a few minutes after the low-level mesocyclone (centered at ~1 km AGL) intensified. After the tornado appeared visually, $\Delta V_{\max}$ suddenly (i.e., within the temporal resolution of the volume scans) increased from 500 m up to 3 km and near the ground. The vortex diameter contracted first from near the ground up to 500 m and a few minutes later up to the top of the domain. *It thus appears that the tornado began near the ground, possibly in response to the intensification of the low-level mesocyclone and then built upward with time in discrete bursts.*

b. *The later part of D2 (2307–2314 UTC): The development of a violent tornado*

During the second part of D2 the volume sampled by RaXPol extended only up to ~750 m AGL at the beginning of the adjusted scanning strategy (2307:00 UTC), and decreased to only ~400 m AGL at the end of the stationary part of D2, as the tornado approached the location of the radar and data collection became mobile (Fig. 7; the reader should note that different color scales are used in Figs. 5 and 7 to accommodate the higher values of $\Delta V_{\max}$ and ζ_{pseudo} and lower values of D in the latter). The highest $\Delta V_{\max}$ continued to be right near the ground, below ~100 m AGL. The tornado weakened a little around 2308:00 UTC, as $\Delta V_{\max}$ decreased slightly and D increased to >1.5 km between 100 and 500 m AGL, possibly owing to the attempted development of a central downdraft as in Ward (1972). However, beginning ~2310:00 UTC, the tornado near the ground reintensified until about 2313:00 UTC, when another burst of rapid intensification ($\Delta V_{\max}$ > 10–20 m s^{-1} in ~15–20 s) occurred: $\Delta V_{\max}$ increased to > 130 m s^{-1} over the depth of the volume (~400 m deep) and the diameter of the vortex contracted to < 250 m. At this time ζ_{pseudo} increased in the lowest 150 m and separately, above ~200 m AGL; by 2314:00 UTC, however, the increase in ζ_{pseudo} to > 1 s^{-1} was continuous from the ground up to the top of the volume (~450 m). The reader is cautioned, however, that the decrease in D and resulting increase in ζ_{pseudo} may be caused at least in part by the increase in spatial resolution of the Doppler data as the range to the tornado decreased with time during the deployment. When the core diameter shrank, the tornado was still in the early stages of its evolution; it became much wider later, around and after 2325 UTC (Bluestein et al. 2015, see, e.g., their Figs. 17 and 19).

c. *Vertical cross sections through the tornado*

Vertical cross sections through the tornado were obtained via objective analysis of RaXPol data normal

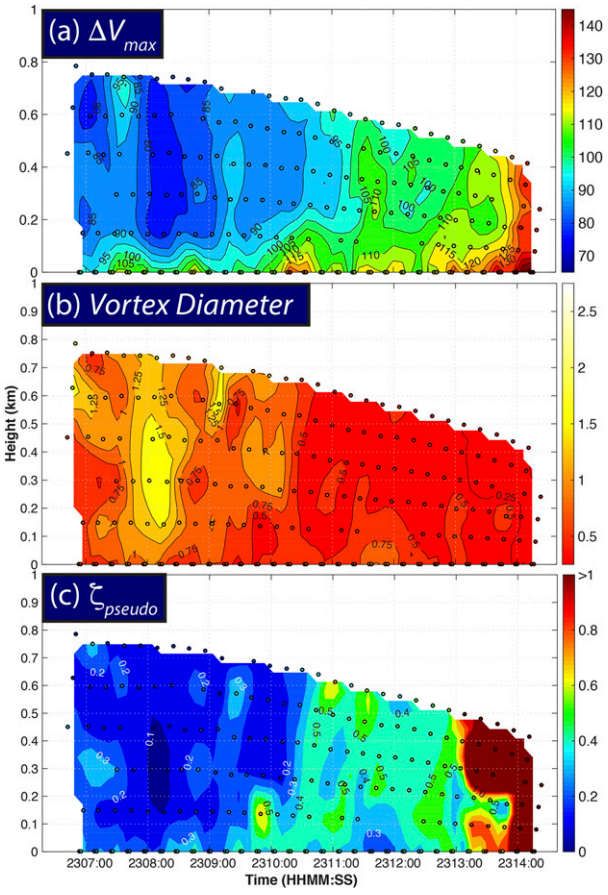

FIG. 7. As in Fig. 5, but for the second half of D2, for early tornado evolution. Range to the TVS was ~4.5–8.5 km.

to the radar beam at the location that the beam intersected the center of the tornado at the 0° elevation angle. These vertical cross sections graphically illustrate certain aspects of the tornado structure as it evolved (on time scales >10–20 s, the time between successive volume scans), such as tilt with height (generally in the north–south plane), the variation of the winds with height, and the development of a weak-echo column (WEC; Tanamachi et al. 2012).

1) DOPPLER VELOCITY

The vortex tilted toward the north with height, becoming even more tilted overall in the lowest 2 km after tornadogenesis (Fig. 8). This additional overall tilt with height might have occurred because the tornado near the ground formed to the south of the vortex aloft; at 2303:43 UTC (Figs. 8d, 9), the TVS in the lowest 500 m appeared to be distinct from the TVS vortex signature aloft. In the lowest several hundred m, however, the vortex was nearly vertically erect.

Just prior to tornadogenesis, the center of rotation 0–100 m AGL (0° elevation angle) propagated to the south-southwest while the center of rotation aloft, 3–4 km AGL (20° elevation angle), propagated to the west-southwest, in the direction opposite to that of storm motion (Fig. 9). The distance between the centers of rotation between the upper and lower layers doubled from 1 km at 2300:50–2301:15 UTC to 2 km at 2302:17–2302:42 UTC.

2) WEC

A zoomed-in view of the vertical cross section valid at 2305:39 UTC in Fig. 8 is shown in Fig. 10. The WEC and vortex signature are nearly erect in the lowest 750 m, but tilt toward the north up to 2.5 km at about a 45° angle [the vortex signature actually tilted to the north-northwest with height (Fig. 9)]. Tilted tornadoes are commonly observed visually and on radar, especially as the tornado dissipates and a gust front upends the vortex near the ground (e.g., Bluestein 2013; French et al. 2014). Bluestein (2019, his Fig. 24), for example, has documented a dissipating tornado for which part is actually completely horizontal during dissipation. Wurman and Kosiba (2013) have also documented a horizontal vortex in a tornadic supercell. Tilted tornadoes, however, have also been documented during tornadogenesis as well (e.g., French et al. 2014) and therefore do not necessarily mean that the tornado is about to dissipate. In this case, the separation between the near-surface vortex and the low-level mesocyclone did not decrease before the tornado intensified throughout the column (Fig. 8).

As the tornado intensified (Fig. 11), the WEC extended from the lowest elevation angle up to the top of the domain ~800 m AGL most of the time, but beginning at 2309:01 UTC retreated upward, where the 30-dBZ contour had lifted to as high as 300 m AGL or more (e.g., at 2310:04 UTC it was higher than 4 km AGL). Houser et al. (2016) noted similar behavior in the El Reno tornado in 2011. The WEC had broadened to over 500 m in width by 2312:10 UTC, but then disappeared, save for an annular WEC at ~500-m radius at and after 2313:45 UTC. One possible explanation for the annular WEC is that a central downdraft penetrated through the WEC, splitting it and causing it to propagate radially outward (the distance between the outer edges of the WEC at 2313:13 UTC was less than the distance between the outer limits of the annulus of WEC at 2314:00 UTC). Alternatively, it is possible that the central downdraft at low levels simply weakened at the center of the tornado; however, evidence for this in the Doppler velocity field (Fig. 12) is

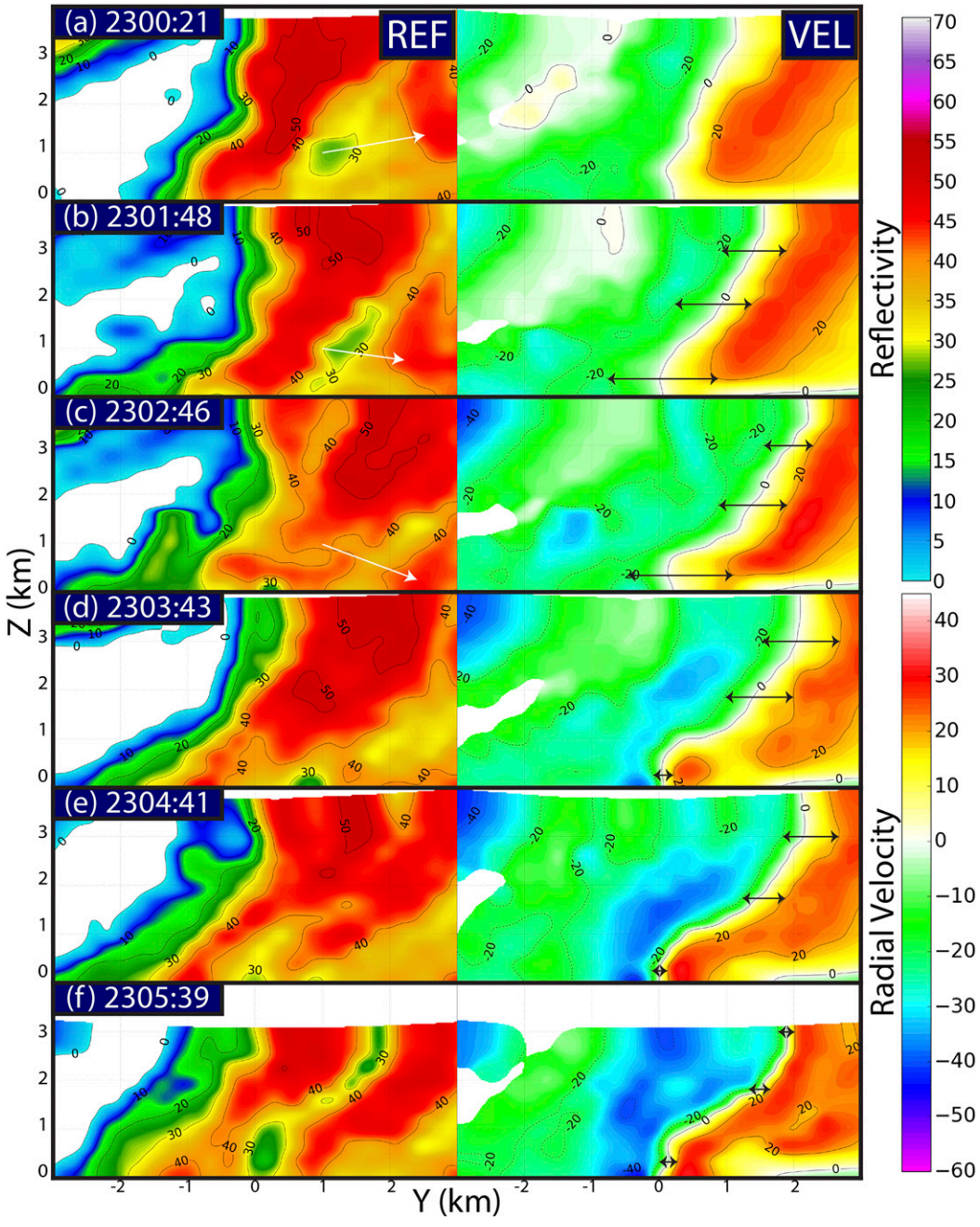

FIG. 8. Evolution of vertical cross sections in the north–south direction (y increases to the north and is zero at the location of the TVS near the surface; Z is the height ARL) of the (left) interpolated radar reflectivity factor (dBZ) and (right) dealiased Doppler velocity (m s^{-1}), from RaXPol, (a)–(f) during tornadogenesis and early tornado evolution (at the times indicated in UTC on 31 May 2013) given by the TVS. The double arrows indicate the separation distance between the −20 and +20 m s^{-1} isodops; it is seen how the separation distances decrease with time. The white arrows point to a descending 40-dBZ core just north of the tornado. Range to the TVS was ~8.75–9 km.

not apparent. It is possible that the WEC retreated upward because the tornado weakened around 2308 UTC (Fig. 5a) and the diameter of the vortex signature increased (Figs. 5b, 12). At and after 2313: 13 UTC, however, the WEC retreated up to 300 m AGL, while the Doppler shear intensified and reflectivity below the WEC became stronger. At this time, damage indicators associated with higher wind

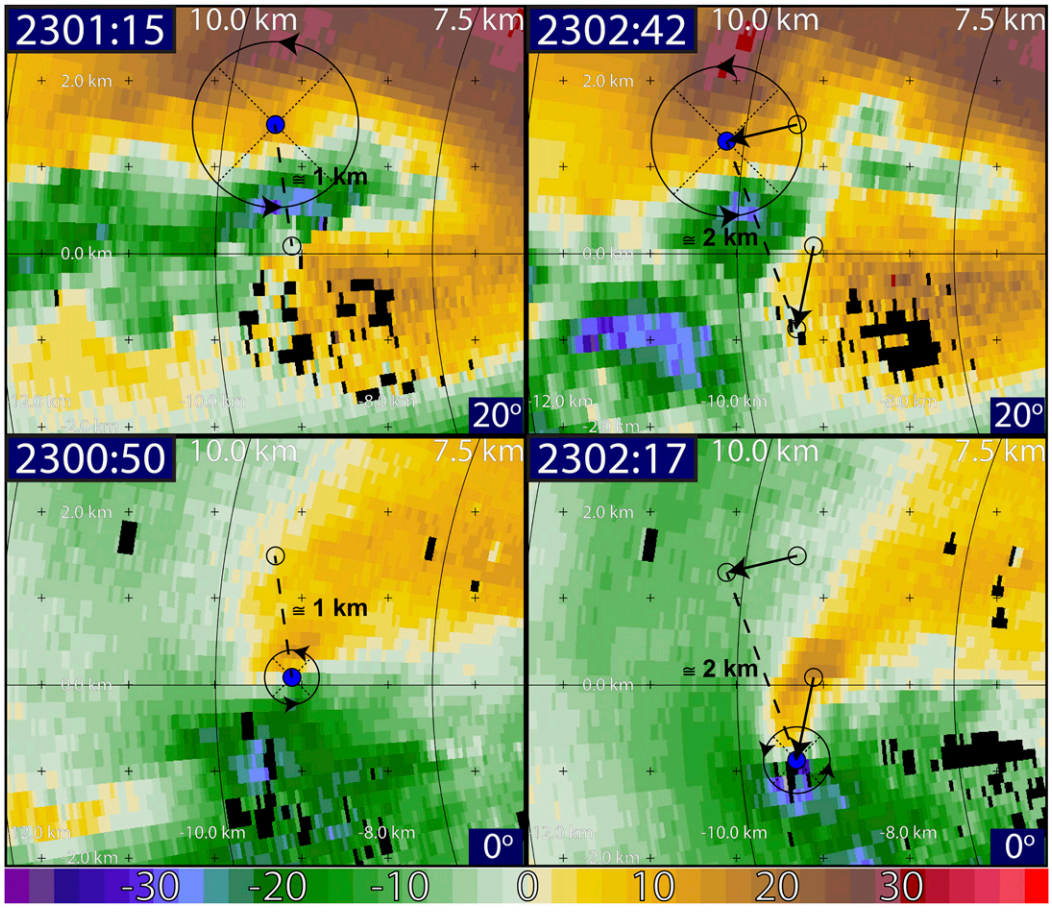

FIG. 9. Illustration of how the tilt of the TVSs with height changes with time during part of D2. Doppler velocities (m s^{-1}) in sector of PPIs at (bottom) 0° elevation angle and (top) 20° elevation angle (~800 m AGL), from RaXPol data. Range markers are shown every 2.5 km. Times plotted in UTC on 31 May 2013. Blue dots indicate locations of TVS at all four times, at different elevation angles; black rings with arrows (indicating direction of the flow) and cross hairs indicate TVS locations only for the times and elevation angle indicated in each panel. Small circles in panels on the left indicate TVS locations above and below; additional small circles in panels on the right also indicate locations of the corresponding TVS locations on the left, at the earlier time. Arrows connecting TVS locations indicate direction and speed of motion of TVSs at each elevation angle (on rightmost panels). Dashed lines indicate approximate separation of the TVSs at 20° elevation angle form those at 0° elevation angle.

speeds were documented (Marshall et al. 2014; Wakimoto et al. 2016), so it is likely that the WEC retreated upward at this time because more debris was lofted. To verify this hypothesis, we consider polarimetric data.

The debris signature in the tornado represented by relatively low copolar cross-correlation coefficients (ρ_{hv}) and low differential reflectivity (Z_{DR}) (not shown), as located by the regions of $\rho_{hv} < 0.6$, expanded upward from 300 m to the top of the domain at 800 m between 2306:55 UTC and 2308:45 UTC (Fig. 13). By 2311:22 UTC the debris signature below 300 m AGL had widened to ~900 m (from only ~200 m at 2308:45 UTC), and, at 2312:26 UTC, lobes of reduced ρ_{hv} appeared below 300 AGL. By 2313:29 UTC ρ_{hv} had decreased to less than 0.4 below 300 m and less than 0.6 all the way up to the top of the domain (~800 m AGL). This is further evidence that, as the WEC retreated upward, the debris cloud was in fact being advected upward.

From ~2307 to 2309 UTC, the tornado was most intense near the ground, while a broader vortex was located above 100 m (Figs. 5, 12). After ~2310–2311 UTC, the vortex tightened up from near the surface up to the top of the domain. After ~2313 UTC the vortex intensified again throughout the depth of the analysis, but the intensification occurred first near the surface (e.g., at 2312:42 UTC). The

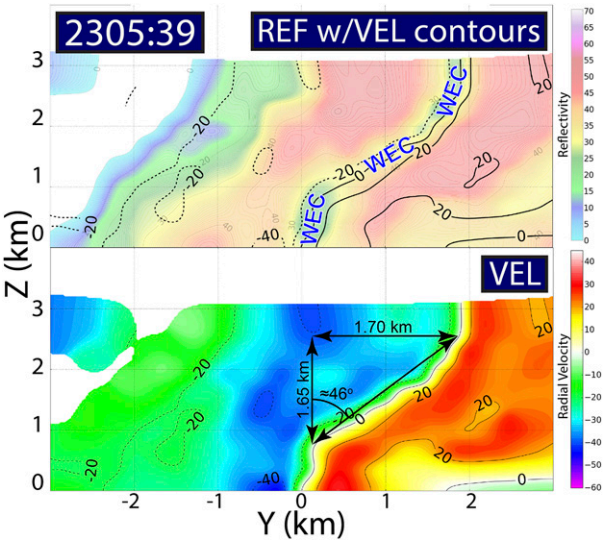

FIG. 10. Illustration of the tilt (triangle shows ΔY, ΔZ, and the hypotenuse) of the tornado when it was intensifying as seen by RaXPol: Vertical cross sections in approximately the north–south direction (y, with $y = 0$ at the tornado near the surface; Z is the height ARL) through the tornado at 2305:39 UTC 31 May 2013 of (top) radar reflectivity factor (dBZ, faded) and Doppler velocity (m s^{-1}) contours (solid lines) and (bottom) Doppler velocity (m s^{-1}). Range to the TVS was ~8.75 km.

intensification phase of the tornado therefore was not steady but, rather, underwent several spurts of growth. Alexander and Wurman (2005) and French et al. (2014) have also reported similar results. Kosiba et al. (2013) found in the analysis of another tornadic storm (the Goshen County supercell during VORTEX-2) that tornado intensification (at low levels) was also not steady.

3) DRCs

Evidence of DRCs (not all shown) in the RFD region of the supercell was found. At least five occurrences of DRCs were observed from 2307–2312 UTC. The best example is of one beginning at 2307:10 UTC and ending ~2307:58 UTC (Fig. 14); it is seen as a descending closed 50-dBZ reflectivity (black arrows) region south of the tornado. In the two scans (~15–30 s later) following the descent to the ground of the 50-dBZ reflectivity, a shift in the location of the maximum inbound velocity near the ground occurred toward the center of the tornadic circulation. Along with this shift, the inbound velocities increased to over 50 m s^{-1} at this time, most likely due to the conservation of angular momentum as the width of the vortex decreased. This increase in tornado intensity following the DRC can also be seen in Fig. 5a around ~2308:30 UTC. Since the rate of descent of the DRC was estimated from the approximate centroid of the 50-dBZ contour-closed curve to be ~10.4 m s^{-1}, which is also approximately the terminal fall velocity of large raindrops (Rogers and Yau 1996, 124–126), the DRC was probably associated with falling precipitation, assuming that it did not fall into a strong updraft or downdraft. Differential reflectivity in the falling precipitation, however, was only moderately high (~2 dB; not shown), which is characteristic of raindrops of diameter ~3 mm (e.g., Seliga and Bringi 1976; Snyder et al. 2010, their Fig. 1), whose fall speeds are less than 10 m s^{-1} (e.g., Spilhaus 1948). The rate of descent of the DRC due to the terminal fall speed of the precipitation could have been augmented by some downward-directed dynamic pressure gradient force near the low-level vortex.

5. Discrete bursts of enhanced precipitation in the right-forward flank

Animations of radar reflectivity (see online supplemental material) were inspected to see if there were any other features that might have been correlated with tornadogenesis. Prior to the formation of the first main tornado, a band of enhanced precipitation at 4° elevation angle (~700 m AGL), an elevation angle that was subjectively determined to be completely free from ground clutter contamination, was noted moving rapidly to the west in the forward flank of the storm, just to the east or northeast of the developing hook echo. This behavior is summarized in Fig. 15, which shows that beginning ~2252:18 UTC, embedded within lighter precipitation, there was a group of parallel, curved bands of enhanced radar reflectivity (the leading edge, with respect to the motion of the group of bands, is marked by black arrows) that appear 7–10 km to the west-southwest of RaXPol. The leading edge of the bands was oriented initially in the north–south direction, but it rotated cyclonically into the northwest–southeast direction by 2254:42 UTC and then propagated westward into the region of the developing hook (west of the 10-km range marker) about the time that Doppler shear of tornadic intensity appeared at the surface (Fig. 4a). This apparent enhancement of precipitation did *not* appear, however, to be associated with a downdraft (no convergence signature is seen near it at low altitudes; not shown), that could have intensified convergence in the area near where the hook echo and tornado subsequently appeared or if this evolution is purely coincidental with hook echo development.

A similar sequence of events was noted several minutes later (Fig. 16): Enhanced radar reflectivity (brown) embedded within lighter precipitation was

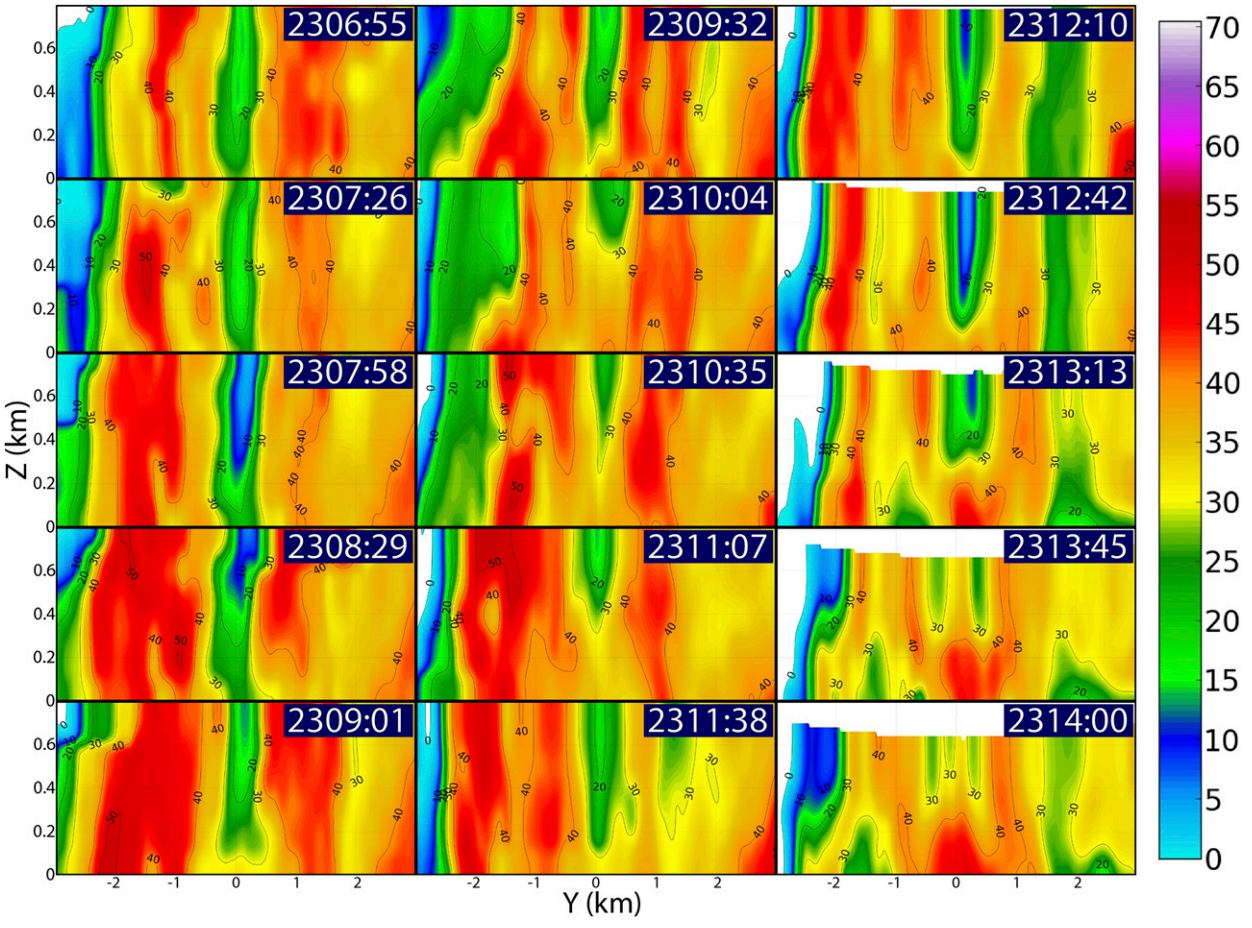

FIG. 11. Evolution of the radar reflectivity (dBZ) structure of the tornado as seen by RaXPol during the second part of D2. Vertical cross sections in the north–south direction (y, with $y = 0$ at the tornado at the surface; Z is the height ARL) initially, turning gradually to approximately the northwest–southeast direction at the end of the series, of radar reflectivity (dBZ), at ~30-s intervals (times shown in UTC, 31 May 2013). Range to the TVS was ~8–9 km.

first evident at 2300:00 UTC to the east of the developing hook. The leading edge, with respect to radar-echo motion, of a group of parallel, curved bands of enhanced precipitation (leading edge marked by a black arrow) formed and rotated cyclonically, eventually merging with the developing hook echo around 2302:24 UTC. In addition, a stronger (i.e., $Z >$ 60 dBZ) band of precipitation appears to the northwest of the bands of enhanced precipitation, adjacent and to the south of the concaved edge of precipitation associated with the supercell. Again, there was no evidence of enhanced low-level convergence (not shown).

In both of the aforementioned bursts of precipitation in the right-forward flank of the supercell, no corresponding changes in the Doppler velocity field were noted at 4° elevation angle or at the ground (not shown). The differential reflectivity during each burst was as high as ~4.5 dB at 4° elevation angle (Fig. 17), which corresponds to water droplets ~6 mm in diameter (Snyder et al. 2010, their Fig. 1). The bands of higher reflectivity did not appear to be well correlated with the bands of differential reflectivity seen in Fig. 17.

If the two aforementioned episodes of the appearance of precipitation bands at low levels in the right-forward flank of the supercell play any causal role in the development of the tornado, then this might be evidence of a developing reflectivity core in the *right-forward* flank of the storm, which propagates against the direction of storm motion as it is embedded within the very broad circulation of the storm, as opposed to previously described DRCs, which appear in the *right-rear* flank (Rasmussen et al. 2006). The authors are unaware of any similar observations in other tornadic supercells, though it might be that previous cases were not inspected carefully enough in the forward-front flank. However,

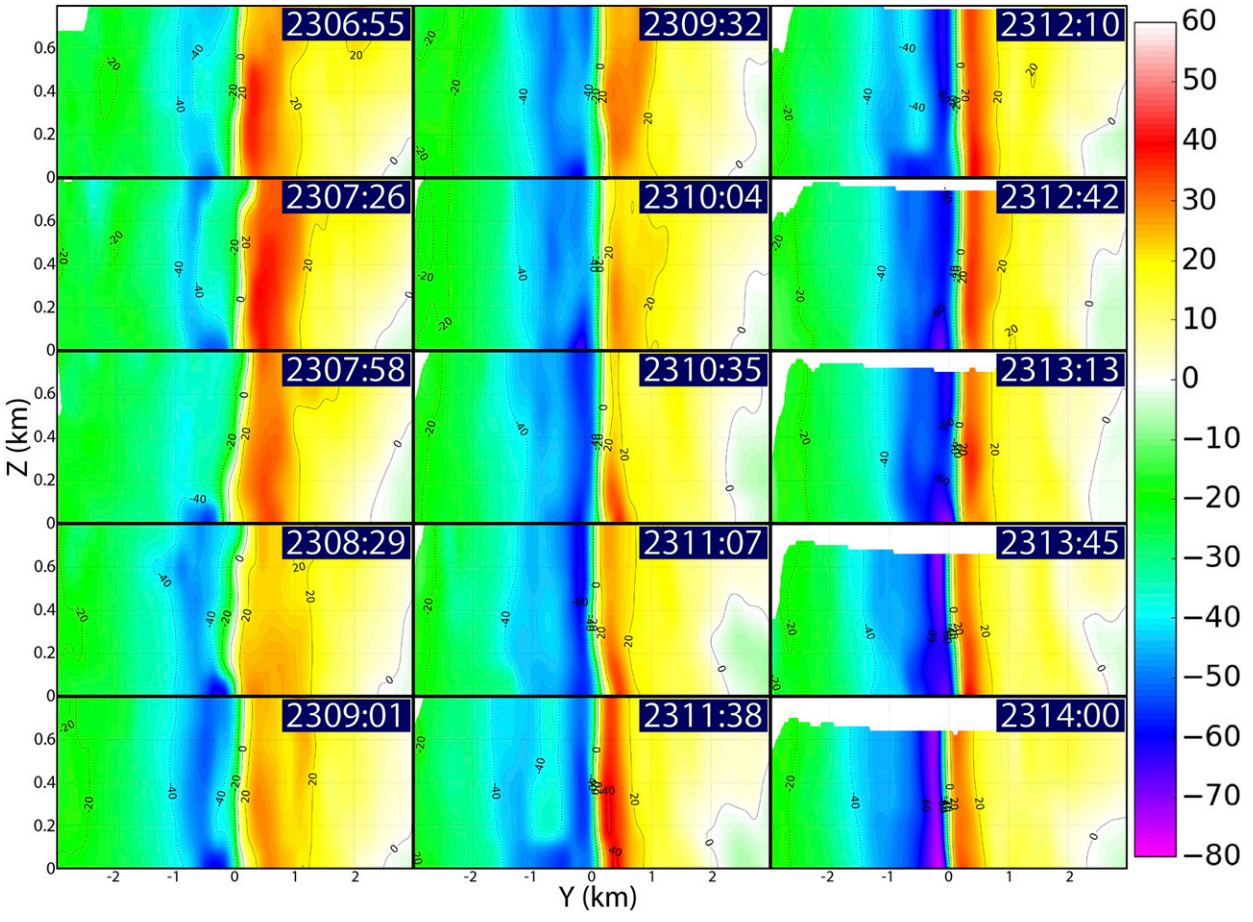

FIG. 12. As in Fig. 11, but for Doppler velocity ($m\,s^{-1}$).

since the right-forward-flank enhancements of precipitation do not appear to descend or influence the surface divergence field, they appear to be different from DRCs.

6. Summary and conclusions

The data from RaXPol used to study the development and evolution of the El Reno tornadic supercell of 31 May 2013 was unprecedented in its spatiotemporal resolution. The tornado was historic in both intensity and size; its parent storm produced phenomena very rarely, if ever before, documented at such high temporal and spatial resolution. The analysis of this case adds to our growing number of cases for which tornadogenesis was observed at close range by mobile, rapid-scan Doppler radars. It is just one of only several, however, for which the tornado produced winds sampled by the radar that are potentially consistent with those associated with EF-5 intensity (at least based on radar data alone) (Burgess et al. 2002; Alexander and Wurman 2005; Wurman et al. 2007, 2014; Snyder and Bluestein 2014; Houser et al. 2015).

The most significant findings are as follows:

1) *Tornadogenesis.* The tornado began first at low levels, but it was preceded by a vortex associated with it at ~1 km AGL (i.e., low-level mesocyclone) that was stronger. This finding is consistent with the hypothesis that a low-level mesocyclone may induce upward motion below, owing to an upward-directed perturbation pressure gradient force (Wicker and Wilhelmson 1995). Coffer and Parker (2015, 2018) and Coffer et al. (2017) have demonstrated, using numerical experiments, the importance of this dynamically induced upward motion underneath robust low-level mesocyclones in tornadogenesis, especially as related to low-level vertical shear in the environment. An increase in vorticity in the friction layer below may be induced through frictional convergence acting on the existing vorticity (e.g., Rotunno 2013); however, the source for that vorticity is currently unknown.

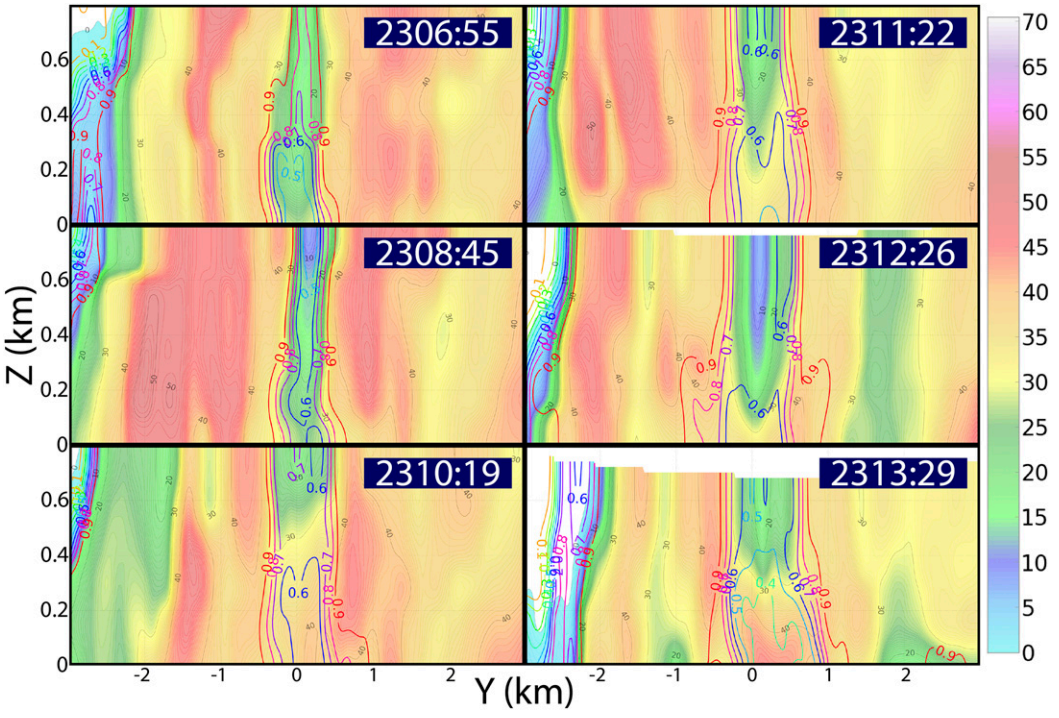

FIG. 13. Evolution of the debris signature in the El Reno tornado during the second part of D2 as detected by RaXPol. As in Fig. 11, but with ρ_{hv} (contours) and radar reflectivity, faded and at less-frequent intervals. Range to the TVS was ~7.5–9 km.

2) *Vertical development of tornado.* The TVS was weaker at ~500 m AGL than it was at lower or higher altitudes just prior to and during the initial stages of tornadogenesis, but, within one scan interval (~20 s), built upward to ~3 km AGL. This rapid upward development means that surveillance radars such as the WSR-88D, which have volume scan times of ~5–6 min, would not be able to detect the full evolution of tornadogenesis [consistent with French et al. (2013) among others]. The nearly simultaneous intensification of the TVS above the ground (Houser et al. 2015) could be a result of the simultaneous contraction of the TVS diameter aloft following a rapid reduction in the diameter of the velocity couplet near the ground, owing to convergence associated with a sudden increase in the strength of an updraft aloft. French et al. (2013) and Houser et al. (2015) also found that there was a relative minimum in Doppler shear at relatively low levels, but above the surface, and that a TVS can propagate upward very rapidly. There are a few possible explanations for the relative minimum in shear: It might be a result of the inhibition of vertical motion as a result of a capping inversion in the environment of the storm [Fig. 6a in Bluestein et al. (2015)]. Alternatively, the relative minimum might be a consequence of the superposition of upward motion above the level of free convection and the upward motion induced by the vertical pressure-gradient force below (Markowski et al. 2012a; French et al. 2013, 2014; Houser et al. 2015). If this were the case, then the rate of change with height of vertical velocity could be reduced just below the LFC and hence there would be a reduction in both convergence and generation of vorticity there. Again, as in other studies, no evidence was found of a descending TVS as predicted by the dynamic pipe effect. The sudden increase in strength of the vortex near the ground is probably a result of boundary layer dynamics (Rotunno 2013).

3) *Relationship between the WEH and the WEC and the vortex.* Although the WEH and WEC can be signs of strong rotation, the absence of each does not necessarily imply that the vortex is weak or not present. In fact, the vortex may be intensifying, but the lofting of debris or the convergence of debris in the surface friction layer may make the WEH disappear near the ground (e.g., Bluestein et al. 2007).

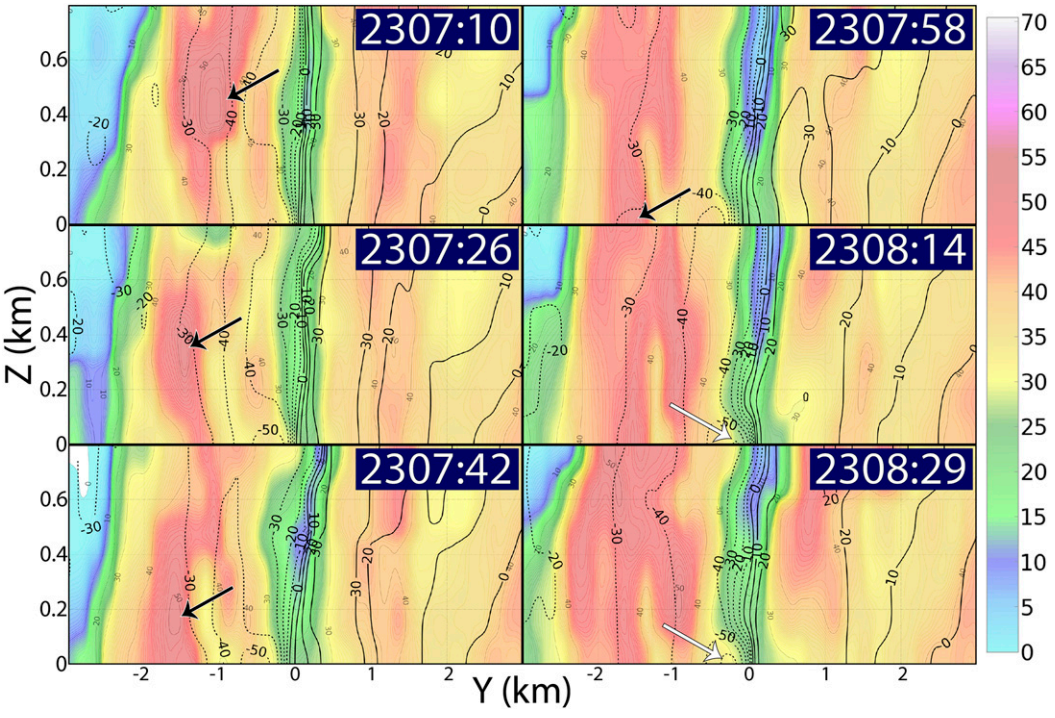

FIG. 14. Evolution of the Doppler wind field (contours, m s^{-1}) and radar reflectivity (color coded, dBZ) during a DRC (black arrows point to 50-dBZ contours), in a vertical plane aligned approximately in the north–south direction, for the times indicated in UTC, on 31 May 2013. White arrows point to the corresponding increase in Doppler velocity near the ground, on the southern side of the tornado. Range to the TVS was ~8.5 km.

4) *Tilt of the tornado.* The 2013 El Reno tornado was highly tilted above the lowest 500 m when it was intensifying. As noted by French et al. (2014), the tilt of a tornado does not necessarily imply that it is dissipating. The reason why a tornado has some tilt when it is intensifying is probably different from the reason why it tilts when it is dissipating: In the latter case, the gust front associated with the storm's cold pool probably forces the surface tornado in a different direction from that of storm motion (Snook and Xue 2008). In the former case, however, the differential motion of the midlevel mesocyclone and low-level mesocyclone could be responsible for the tilt because the physical processes responsible for the formation of each are different (tilting of midlevel horizontal vorticity versus baroclinic generation along the forward flank near the ground, followed by tilting) and acting in different locations. Furthermore, the additional separation of the low-level and midlevel circulations may act to enhance the stretching (by increasing the length of the vortex and also tilting it onto the horizontal) and intensification of the preexisting vortex, acting to amplify tornadogenesis. Markowski and Richardson (2014), however, have argued that when the low- and midlevel circulations are displaced from each other, the surface vortex is displaced from the region of dynamic lifting and hence tornadogenesis is *not* favored.

5) *Relationship between downdrafts and tornado intensification.* The intensification of the vortex at low- and midlevels does not proceed at a uniform pace. It is hypothesized that discrete surges of momentum near the ground, which are associated with downdrafts, could be responsible for this behavior (e.g., Kosiba et al. 2013; Marquis et al. 2016). DRCs have been associated with vortex intensification (Markowski et al. 2012a,b) and downdrafts accompanying them could cause the surges. In the case of the 31 May 2013 El Reno tornado, the tornado did intensify following a DRC, but no direct evidence linking the DRC to a downdraft is seen, though increased surface convergence is evident. The development of surges could also be responsible for the tilt of the tornado/separation of the midlevel and low-level vortices, as the low-level vortex is shifted away from the location of the midlevel vortex (Snook and Xue 2008).

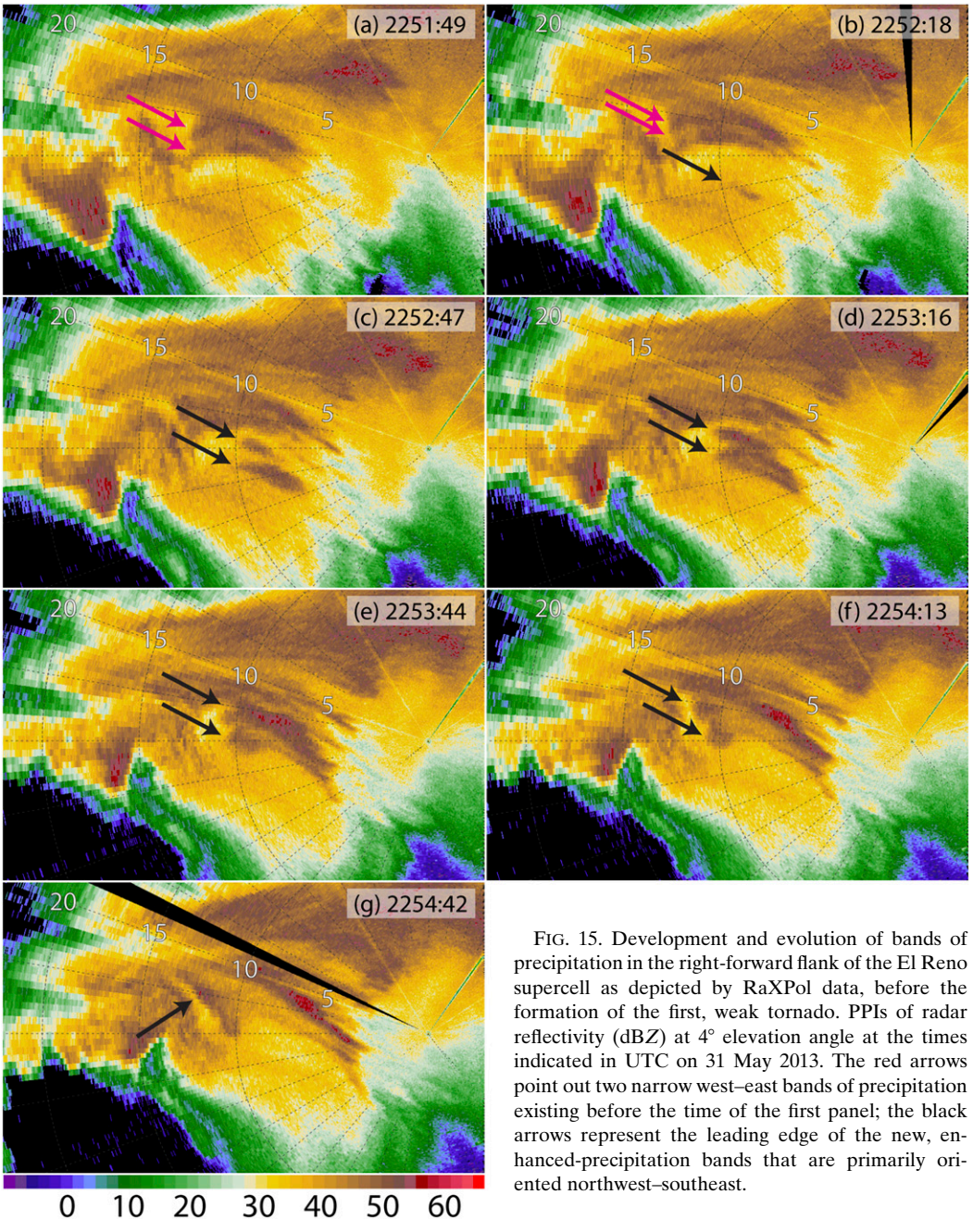

FIG. 15. Development and evolution of bands of precipitation in the right-forward flank of the El Reno supercell as depicted by RaXPol data, before the formation of the first, weak tornado. PPIs of radar reflectivity (dBZ) at 4° elevation angle at the times indicated in UTC on 31 May 2013. The red arrows point out two narrow west–east bands of precipitation existing before the time of the first panel; the black arrows represent the leading edge of the new, enhanced-precipitation bands that are primarily oriented northwest–southeast.

6) *Relationship between precipitation in the right-forward flank and tornado intensification.* Evidence was presented that bands of enhanced precipitation in an area of light-to-moderate precipitation that fell in the right-forward flank of the storm occurred while the vortex was intensifying. This may be the first time that reflectivity cores appearing in the forward flank have been documented during tornadogenesis. Evaporation might be enhanced as heavier precipitation falls into unsaturated air, leading to more cooling and a stronger baroclinic zone along the edge of the forward-flank downdraft, thus allowing for greater baroclinic generation (Rotunno and Klemp 1985) of low-level vorticity. If this explanation is correct, then it could explain the bottom-up view of tornadogenesis in terms of the importance of the production of a low-level mesocyclone. *In this case, there appears to be a surge of enhanced precipitation into the northern*

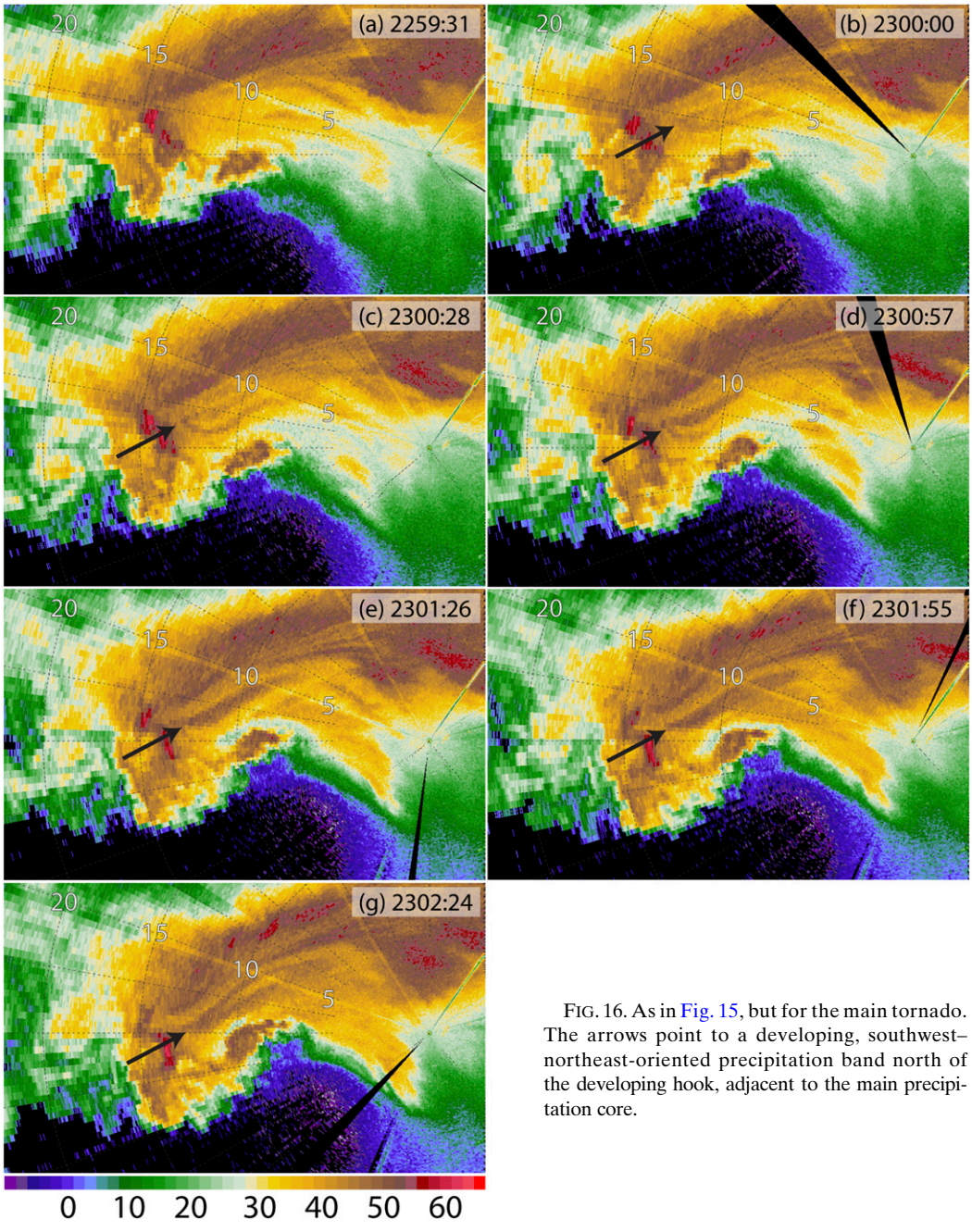

FIG. 16. As in Fig. 15, but for the main tornado. The arrows point to a developing, southwest–northeast-oriented precipitation band north of the developing hook, adjacent to the main precipitation core.

half (in the Northern Hemisphere) of the hook echo region, rather than a surge of precipitation (and outflow) to the rear of the leading edge of the rear-flank gust front. Perhaps other cases should be re-examined to see how common this feature is. It might be that the behavior of these bands of enhanced precipitation is a result of tornado intensification, however, and not a cause, since no evidence of enhanced low-level convergence was found. The effects of enhanced precipitation in the forward flank, on the surface baroclinicity, need to be studied.

A synthesis of an idealized conceptual model of the structures in a tornadic supercell based on many radar reflectivity images, as has been done, for example, for mesoscale convective systems by Parker and Johnson (2000) and by Willoughby et al. (1984) for hurricane rainbands, appears in Fig. 18. This model includes the secondary surges to the rear of the rear-flank gust front (RGFG) and DRCs described in this study, in addition

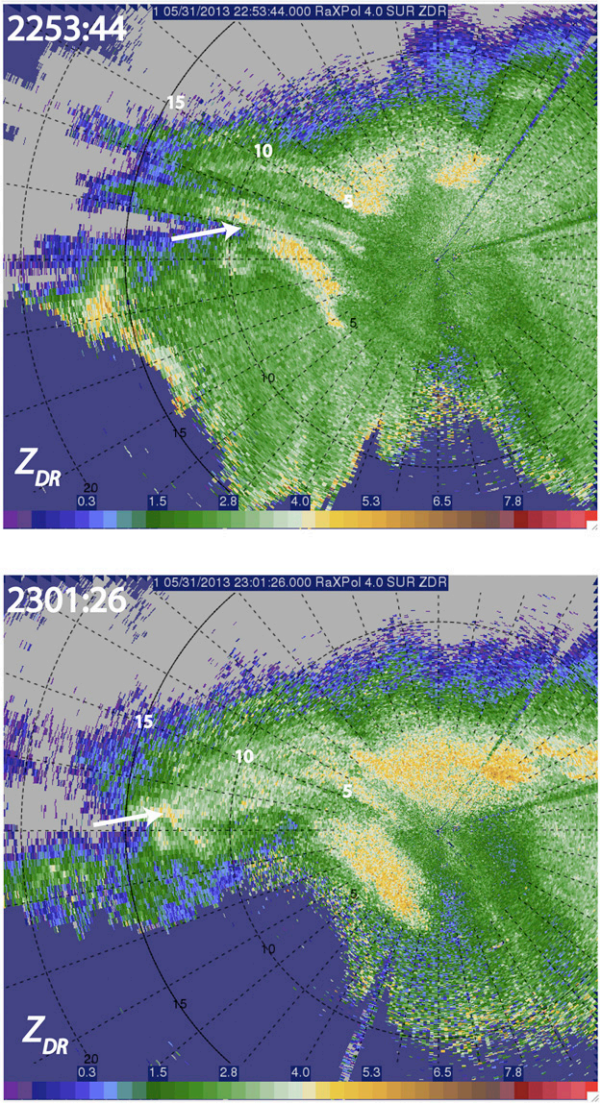

FIG. 17. Differential reflectivity (Z_{DR}) in dB at 4° elevation angle at (a) 2253:44 and (b) 2301:26 UTC 31 May 2013, from RaXPol. Corresponds with radar reflectivity shown in Fig. 15e and Fig. 16e (white arrows point to features of interest). Range markers shown every 5 km.

to the low-reflectivity ribbon (LRR) (e.g., Wurman et al. 2012; Kosiba et al. 2013; Snyder et al. 2013; Griffin et al. 2018), which may mark a region of sparsely populated large hailstones, and weak-echo reflectivity band (WRB; Houser et al. 2016), which is produced by the subsiding branch of a horizontal roll behind an RFGF.

Finally, we need to find out how general our findings are concerning the vertical variation of tornadogenesis. While the evidence is mounting, the sample size of rapid-scan observations from near the ground up to at least 2–3 km AGL in a storm is still relatively small.

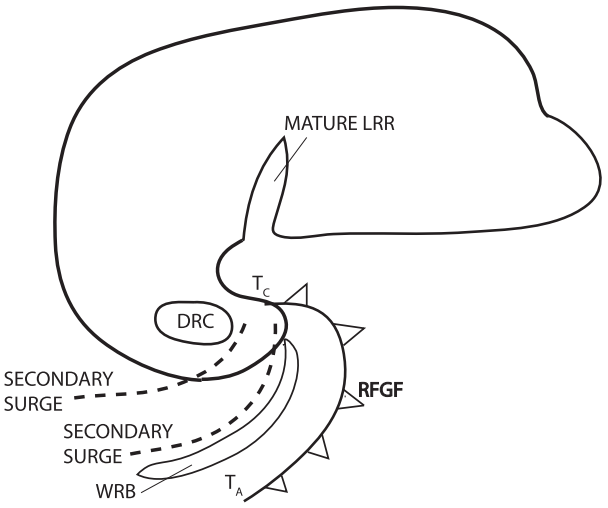

FIG. 18. Idealized plan view model of a tornadic supercell at low altitude showing substorm features such as a mature low-reflectivity ribbon (LRR), a descending reflectivity core (DRC), secondary rear-flank gust front surges (dashed lines), rear-flank gust front (RFGF) (cold-front symbol), cyclonic tornado (T_C), anticyclonic tornado (T_A), and weak reflectivity band (WRB). Not all features are seen in every supercell, nor are they all seen together at any given time. Radar echo outline is ~40–45 dB*Z*; DRC radar echo outline is ~50 dB*Z*.

Acknowledgments. NSF grants AGS-1262048 and AGS-1560945 funded this study. RaXPol was built with support from MRI grant from NSF AGS-0821231. The maintenance of RaXPol is supported by the Advanced Radar Research Center (ARRC) at the University of Oklahoma (OU). We are indebted to John Meier, Tian Yu, and Bob Palmer at the ARRC for their radar support.

REFERENCES

Alexander, C. R., and J. Wurman, 2005: The 30 May 1998 Spencer, South Dakota, storm. Part I: The structural evolution and environment of the tornadoes. *Mon. Wea. Rev.*, **133**, 72–96, https://doi.org/10.1175/MWR-2855.1.

——, and ——, 2008: Updated mobile radar climatology of supercell tornado structures and dynamics. *24th Conf. on Severe Local Storms,* Savannah, GA, Amer. Meteor. Soc., 19.4, https://ams.confex.com/ams/24SLS/techprogram/paper_141821.htm.

Barnes, S. L., 1964: A technique for maximizing details in numerical weather map analysis. *J. Appl. Meteor.*, **3**, 396–406, https://doi.org/10.1175/1520-0450(1964)003<0396:ATFMDI>2.0.CO;2.

Bluestein, H. B., 2013: *Severe Convective Storms and Tornadoes: Observations and Dynamics*. Springer, 456 pp.

——, 2019: Observations of tornadoes and their parent supercells using ground-based, mobile Doppler radars. *Remote Sensing and Natural Disasters, Geophys. Monogr.*, Amer. Geophys. Union, in press.

——, C. C. Weiss, M. M. French, E. M. Holthaus, and R. L. Tanamachi, 2007: The structure of tornadoes near Attica,

Kansas, on 12 May 2004: High-resolution, mobile, Doppler radar observations. *Mon. Wea. Rev.*, **135**, 475–506, https://doi.org/10.1175/MWR3295.1.

——, M. M. French, I. PopStefanija, R. T. Bluth, and J. B. Knorr, 2010: A mobile, phased-array Doppler radar for the study of severe convective storms: The MWR-05XP. *Bull. Amer. Meteor. Soc.*, **91**, 579–600, https://doi.org/10.1175/2009BAMS2914.1.

——, J. C. Snyder, and J. B. Houser, 2015: A multiscale overview of the El Reno, Oklahoma, tornadic supercell of 31 May 2013. *Wea. Forecasting*, **30**, 525–552, https://doi.org/10.1175/WAF-D-14-00152.1.

——, M. M. French, and J. C. Snyder, 2016: Doppler radar observations of anticyclonic tornadoes in cyclonically rotating, right-moving supercells. *Mon. Wea. Rev.*, **144**, 1591–1616, https://doi.org/10.1175/MWR-D-15-0304.1.

——, K. J. Thiem, J. C. Snyder, and J. B. Houser, 2018: The multiple-vortex structure of the El Reno, Oklahoma, tornado on 31 May 2013. *Mon. Wea. Rev.*, **146**, 2483–2502, https://doi.org/10.1175/MWR-D-18-0073.1.

Bringi, V. N., and V. Chandrasekar, 2001: *Polarimetric Doppler Weather Radar*. 1st ed. Cambridge University Press, 636 pp.

Brown, R. A., L. R. Lemon, and D. W. Burgess, 1978: Tornado detection by pulsed Doppler radar. *Mon. Wea. Rev.*, **106**, 29–39, https://doi.org/10.1175/1520-0493(1978)106<0029:TDBPDR>2.0.CO;2.

Burgess, D. W., M. A. Magsig, J. Wurman, D. C. Dowell, and Y. Richardson, 2002: Radar observations of the 3 May 1999 Oklahoma City tornado. *Wea. Forecasting*, **17**, 456–471, https://doi.org/10.1175/1520-0434(2002)017<0456:ROOTMO>2.0.CO;2.

Byko, Z., P. Markowski, Y. Richardson, J. Wurman, and E. Adlerman, 2009: Descending reflectivity cores in supercell thunderstorms observed by mobile radars and in a high-resolution numerical simulation. *Wea. Forecasting*, **24**, 155–186, https://doi.org/10.1175/2008WAF2222116.1.

Coffer, B. E., and M. D. Parker, 2015: Impacts of increasing low-level shear on supercells during the early evening transition. *Mon. Wea. Rev.*, **143**, 1945–1969, https://doi.org/10.1175/MWR-D-14-00328.1.

——, and ——, 2018: Is there a ''tipping point'' between simulated nontornadic and tornadic supercells in VORTEX2 environments? *Mon. Wea. Rev.*, **146**, 2667–2693, https://doi.org/10.1175/MWR-D-18-0050.1.

——, ——, J. M. L. Dahl, L. J. Wicker, and A. J. Clark, 2017: Volatility of tornadogenesis: An ensemble of simulated nontornadic and tornadic supercells in VORTEX2 environments. *Mon. Wea. Rev.*, **145**, 4605–4625, https://doi.org/10.1175/MWR-D-17-0152.1.

Dahl, J. M. L., 2015: Near-ground rotation in simulated supercells: On the robustness of the baroclinic mechanism. *Mon. Wea. Rev.*, **143**, 4929–4942, https://doi.org/10.1175/MWR-D-15-0115.1.

——, M. D. Parker, and L. J. Wicker, 2014: Imported and storm-generated near-ground vertical vorticity in a simulated supercell. *J. Atmos. Sci.*, **71**, 3027–3051, https://doi.org/10.1175/JAS-D-13-0123.1.

Doviak, R. J., and D. S. Zrnić, 1993: *Doppler Radar and Weather Observations*. 2nd ed. Academic Press, 562 pp.

Dowell, D. C., C. R. Alexander, J. M. Wurman, and L. J. Wicker, 2005: Centrifuging of hydrometeors and debris in tornadoes: Radar-reflectivity patterns and wind-measurement errors. *Mon. Wea. Rev.*, **133**, 1501–1524, https://doi.org/10.1175/MWR2934.1.

French, M. M., H. B. Bluestein, I. PopStefanija, C. A. Baldi, and R. T. Bluth, 2013: Reexamining the vertical development of tornadic vortex signatures in supercells. *Mon. Wea. Rev.*, **141**, 4576–4601, https://doi.org/10.1175/MWR-D-12-00315.1.

——, ——, ——, ——, and ——, 2014: Mobile, Phased-array, Doppler radar observations of tornadoes at X band. *Mon. Wea. Rev.*, **142**, 1010–1036, https://doi.org/10.1175/MWR-D-13-00101.1.

Griffin, C. B., C. C. Weiss, A. E. Reinhart, J. C. Snyder, H. B. Bluestein, J. Wurman, and K. A. Kosiba, 2018: In situ and radar observations of the low reflectivity ribbon in supercells during VORTEX2. *Mon. Wea. Rev.*, **146**, 307–327, https://doi.org/10.1175/MWR-D-17-0201.1.

Houser, J. L., H. B. Bluestein, and J. C. Snyder, 2015: Rapid-scan, polarimetric, Doppler radar observations of tornadogenesis and tornado dissipation in a tornadic supercell: The ''El Reno, Oklahoma'' storm of 24 May 2011. *Mon. Wea. Rev.*, **143**, 2685–2710, https://doi.org/10.1175/MWR-D-14-00253.1.

——, ——, and ——, 2016: A finescale radar examination of the tornadic debris signature and weak-echo reflectivity band associated with a large, violent tornado. *Mon. Wea. Rev.*, **144**, 4101–4130, https://doi.org/10.1175/MWR-D-15-0408.1.

Kennedy, A., J. M. Straka, and E. N. Rasmussen, 2007: A statistical study of the association of DRCs with supercells and tornadoes. *Wea. Forecasting*, **22**, 1191–1199, https://doi.org/10.1175/2007WAF2006095.1.

Kosiba, K. A., J. Wurman, Y. Richardson, P. Markowski, P. Robinson, and J. Marquis, 2013: Genesis of the Goshen County, Wyoming, tornado on 5 June 2009 during VORTEX2. *Mon. Wea. Rev.*, **141**, 1157–1181, https://doi.org/10.1175/MWR-D-12-00056.1.

Kurdzo, J. M., and Coauthors, 2017: Observations of severe local storms and tornadoes with the Atmospheric Imaging Radar. *Bull. Amer. Meteor. Soc.*, **98**, 915–935, https://doi.org/10.1175/BAMS-D-15-00266.1.

Liou, Y.-C., H. B. Bluestein, M. M. French, and Z. B. Wienhoff, 2018: Single-Doppler velocity retrieval of the wind field in a tornadic supercell using mobile, phased-array, Doppler radar data. *J. Atmos. Oceanic Technol.*, **35**, 1649–1663, https://doi.org/10.1175/JTECH-D-18-0004.1.

Majcen, M., P. Markowski, Y. Richardson, D. Dowell, and J. Wurman, 2008: Multipass objective analyses of Doppler radar data. *J. Atmos. Oceanic Technol.*, **25**, 1845–1858, https://doi.org/10.1175/2008JTECHA1089.1.

Markowski, P. M., and Y. P. Richardson, 2014: The influence of environmental low-level shear and cold pools on tornadogenesis: Insights from idealized simulations. *J. Atmos. Sci.*, **71**, 243–275, https://doi.org/10.1175/JAS-D-13-0159.1.

——, ——, J. Marquis, J. Wurman, K. Kosiba, P. Robinson, and D. C. Dowell, 2012a: The pretornadic phase of the Goshen county, Wyoming, supercell of 5 June 2009 intercepted by VORTEX2. Part I: Evolution of kinematic and surface thermodynamic fields. *Mon. Wea. Rev.*, **140**, 2887–2915, https://doi.org/10.1175/MWR-D-11-00336.1.

——, and Coauthors, 2012b: The pretornadic phase of the Goshen County, Wyoming, supercell of 5 June 2009 intercepted by VORTEX2. Part II: Intensification of low-level rotation. *Mon. Wea. Rev.*, **140**, 2916–2938, https://doi.org/10.1175/MWR-D-11-00337.1.

Marquis, J., R. Richardson, J. Wurman, and P. Markowski, 2008: Single- and dual-Doppler analysis of a tornadic vortex and surrounding storm-scale flow in the Crowell, Texas, supercell of 30 April 2000. *Mon. Wea. Rev.*, **136**, 5017–5043, https://doi.org/10.1175/2008MWR2442.1.

——, Y. Richardson, P. Markowski, J. Wurman, K. Kosiba, and P. Robinson, 2016: An investigation of the Goshen County, Wyoming, tornadic supercell of 5 June 2009 using EnKF

assimilation of mobile mesonet and radar observations collected during VORTEX2. Part II: Mesocyclone-scale processes affecting tornado formation, maintenance, and decay. *Mon. Wea. Rev.*, **144**, 3441–3463, https://doi.org/10.1175/MWR-D-15-0411.1.

Marshall, T. P., D. Burgess, G. Garfield, J. Snyder, R. Smith, D. Speheger, and H. Bluestein, 2014: Ground-based damage survey and radar analysis of the El Reno, Oklahoma tornado. *27th Conf. on Severe Local Storms,* Madison, WI, Amer. Meteor. Soc., 13.1, https://ams.confex.com/ams/27SLS/webprogram/Paper254342.html.

Oye, R., C. Mueller, and S. Smith, 1995: Software for radar translastion, visualization, editing, and interpolation. Preprints, *29th Conf. on Radar Meteorology*, Vail, CO, Amer. Meteor. Soc., 359–361.

Parker, M. D., and R. H. Johnson, 2000: Organizational modes of midlatitude mesoscale convective systems. *Mon. Wea. Rev.*, **128**, 3413–3436, https://doi.org/10.1175/1520-0493(2001)129<3413:OMOMMC>2.0.CO;2.

Pazmany, A. L., J. B. Mead, H. B. Bluestein, J. C. Snyder, and J. B. Houser, 2013: A mobile, rapid-scanning, X-band, polarimetric (RaXPol) Doppler radar system. *J. Atmos. Oceanic Technol.*, **30**, 1398–1413, https://doi.org/10.1175/JTECH-D-12-00166.1.

Rasmussen, E. N., J. M. Straka, M. S. Gilmore, and R. Davies-Jones, 2006: A preliminary survey of rear-flank descending reflectivity cores in supercell storms. *Wea. Forecasting*, **21**, 923–938, https://doi.org/10.1175/WAF962.1.

Rogers, R., and M. K. Yau, 1996: *A Short Course in Cloud Physics*. Elsevier, 304 pp.

Rotunno, R., 2013: The fluid dynamics of tornadoes. *Annu. Rev. Fluid Mech.*, **45**, 59–84, https://doi.org/10.1146/annurev-fluid-011212-140639.

——, and J. Klemp, 1985: On the rotation and propagation of simulated supercell thunderstorms. *J. Atmos. Sci.*, **42**, 271–292, https://doi.org/10.1175/1520-0469(1985)042<0271:OTRAPO>2.0.CO;2.

Ryzhkov, A. V., T. J. Schuur, D. W. Burgess, and D. S. Zrnić, 2005: Polarimetric tornado detection. *J. Appl. Meteor.*, **44**, 557–570, https://doi.org/10.1175/JAM2235.1.

Seimon, A., J. T. Allen, T. A. Seimon, S. J. Talbot, and D. K. Hoadley, 2016: Crowdsourcing the El Reno 2013 tornado. *Bull. Amer. Meteor. Soc.*, **97**, 2069–2084, https://doi.org/10.1175/BAMS-D-15-00174.1.

Seliga, T. A., and V. N. Bringi, 1976: Potential use of radar differential reflectivity measurements of orthogonal polarizations for measuring precipitation. *J. Appl. Meteor.*, **15**, 69–76, https://doi.org/10.1175/1520-0450(1976)015<0069:PUORDR>2.0.CO;2.

Skinner, P. S., C. C. Weiss, M. M. French, H. B. Bluestein, P. M. Markowski, and Y. P. Richardson, 2014: VORTEX2 observations of a low-level mesocyclone with multiple internal rear-flank downdraft momentum surges in the 18 May 2010 Dumas, Texas, supercell. *Mon. Wea. Rev.*, **142**, 2935–2960, https://doi.org/10.1175/MWR-D-13-00240.1.

Smith, R. K., and L. M. Leslie, 1978: Tornadogenesis. *Quart. J. Roy. Meteor. Soc.*, **104**, 189–199, https://doi.org/10.1002/qj.49710443914.

Snook, N., and M. Xue, 2008: Effects of microphysical drop size distribution on tornadogenesis in supercell thunderstorms. *Geophys. Res. Lett.*, **35**, L24803, https://doi.org/10.1029/2008GL035866.

Snyder, J. C., and H. B. Bluestein, 2014: Some considerations for the use of high-resolution mobile radar data in tornado intensity determination. *Wea. Forecasting*, **29**, 799–827, https://doi.org/10.1175/WAF-D-14-00026.1.

——, ——, G. Zhang, and S. J. Frasier, 2010: Attenuation correction and hydrometeor classification of high-resolution, X-band, dual-polarized mobile radar measurements in severe convective storms. *J. Atmos. Oceanic Technol.*, **27**, 1979–2001, https://doi.org/10.1175/2010JTECHA1356.1.

——, ——, V. Venkatesh, and S. J. Frasier, 2013: Observations of polarimetric signatures in supercells by an X-band mobile Doppler radar. *Mon. Wea. Rev.*, **141**, 3–29, https://doi.org/10.1175/MWR-D-12-00068.1.

Spilhaus, A. F., 1948: Raindrop size, shape and drop fall speed. *J. Meteor.*, **5**, 108–110, https://doi.org/10.1175/1520-0469(1948)005<0108:RSSAFS>2.0.CO;2.

Tanamachi, R. L., H. B. Bluestein, J. B. Houser, S. J. Frasier, and K. M. Hardwick, 2012: Mobile, X-band, polarimetric Doppler radar observations of the 4 May 2007 Greensburg, Kansas, tornadic supercell. *Mon. Wea. Rev.*, **140**, 2103–2125, https://doi.org/10.1175/MWR-D-11-00142.1.

Thiem, K. J., 2016: Rapid-scan, polarimetric, mobile, Doppler-radar observations of the formation, evolution, and structure of the El Reno Tornado of 31 May 2013. M.S. thesis, School of Meteorology, University of Oklahoma, Norman, OK, 120 pp.

Trapp, R. J., and R. Davies-Jones, 1997: Tornadogenesis with and without a dynamic pipe effect. *J. Atmos. Sci.*, **54**, 113–133, https://doi.org/10.1175/1520-0469(1997)054<0113:TWAWAD>2.0.CO;2.

Wakimoto, R. M., N. T. Atkins, K. M. Butler, H. B. Bluestein, K. Thiem, J. Snyder, and J. Houser, 2015: Photogrammetric analysis of the 2013 El Reno tornado combined with mobile X-band polarimetric radar data. *Mon. Wea. Rev.*, **143**, 2657–2683, https://doi.org/10.1175/MWR-D-15-0034.1.

——, and Coauthors, 2016: Aerial damage survey of the 2013 El Reno tornado combined with mobile radar data. *Mon. Wea. Rev.*, **144**, 1749–1776, https://doi.org/10.1175/MWR-D-15-0367.1.

Ward, N. B., 1972: The exploration of certain features of tornado dynamics using a laboratory model. *J. Atmos. Sci.*, **29**, 1194–1204, https://doi.org/10.1175/1520-0469(1972)029<1194:TEOCFO>2.0.CO;2.

Wicker, L. J., and R. B. Wilhelmson, 1995: Simulation and analysis of tornado development and decay within a three-dimensional supercell thunderstorm. *J. Atmos. Sci.*, **52**, 2675–2703, https://doi.org/10.1175/1520-0469(1995)052<2675:SAAOTD>2.0.CO;2.

Willoughby, H. E., F. D. Marks Jr., and R. J. Feinberg, 1984: Stationary and moving convective bands in hurricanes. *J. Atmos. Sci.*, **41**, 3189–3211, https://doi.org/10.1175/1520-0469(1984)041<3189:SAMCBI>2.0.CO;2.

Witt, A., D. Burgess, A. Seimon, J. Allen, J. Snyder, and H. Bluestein, 2018: Rapid-scan radar observations of an Oklahoma tornadic hailstorm producing giant hail. *Wea. Forecasting*, **33**, 1263–1282, https://doi.org/10.1175/WAF-D-18-0003.1.

Wurman, J., and M. Randall, 2001: An inexpensive, mobile, rapid scan radar. Preprints, *30th Int. Conf. on Radar Meteorology*, Munich, Germany, Amer. Meteor. Soc., P3.4, https://ams.confex.com/ams/30radar/techprogram/paper_21577.htm.

——, and K. Kosiba, 2013: Finescale radar observations of tornado and mesocyclone structures. *Wea. Forecasting*, **28**, 1157–1174, https://doi.org/10.1175/WAF-D-12-00127.1.

——, C. Alexander, P. Robinson, and Y. Richardson, 2007: Low-level winds in tornadoes and potential catastrophic tornado impacts in urban areas. *Bull. Amer. Meteor. Soc.*, **88**, 31–46, https://doi.org/10.1175/BAMS-88-1-31.

——, D. Dowell, Y. Richardson, P. Markowski, E. Rasmussen, D. Burgess, L. Wicker, and H. B. Bluestein, 2012: The Second Verification of the Origins of Rotation in Tornadoes Experiment: VORTEX2. *Bull. Amer. Meteor. Soc.*, **93**, 1147–1170, https://doi.org/10.1175/BAMS-D-11-00010.1.

——, K. Kosiba, P. Robinson, and T. Marshall, 2014: The role of multiple-vortex tornado structure in causing storm researcher fatalities. *Bull. Amer. Meteor. Soc.*, **95**, 31–45, https://doi.org/10.1175/BAMS-D-13-00221.1.